Effects of Air Drag and Lunar Third-Body
Pertubrations on Orbital Motion Near
a Reference KAM Torus

THESIS

Luke J. Hagen, Captain, USAF

AFIT/GA/ENY/11-M06

AFIT/GA/ENY/11-M06

EFFECTS OF AIR DRAG AND LUNAR THIRD-BODY
PERTUBRATIONS ON ORBITAL MOTION NEAR
A REFERENCE KAM TORUS

THESIS

Presented to the Faculty

Department of Aeronautics and Astronautics

Graduate School of Engineering and Management

Air Force Institute of Technology

Air University

Air Education and Training Command

In Partial Fulfillment of the Requirements for the

Degree of Master of Science in Astronautical Engineering

Luke J. Hagen, B.S. Aerospace Engineering

Captain, USAF
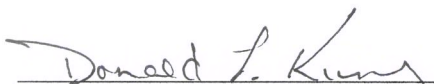
March 2011

AFIT/GA/ENY/11-M06

EFFECTS OF AIR DRAG AND LUNAR THIRD-BODY
PERTUBRATIONS ON ORBITAL MOTION NEAR
A REFERENCE KAM TORUS

Luke J. Hagen, B.S. Aerospace Engineering

Captain, USAF

Approved:

_____
William E. Wiesel, Ph.D. (Chairman)

16 March 2011
_____
Date

_____
Donald L. Kunz, Ph.D. (Member)

16 Mar 2011
_____
Date

_____
Eric D. Swenson, Ph.D. (Member)

15 Mar 2011
_____
Date

AFIT/GA/ENY/11-M06

Abstract

The Kolmogorov, Arnold, and Moser (KAM) Theory was developed in the 1960s but only in the last decade has it been applied to Earth orbiting satellites. Physical state variables of position and velocity are transformed into KAM Torus variables. The KAM Torus is a geometrical structure similar to that of a multi-dimensional donut. The satellite's motion can be described as traversing the surface of this donut. There are two primary advantages of this transformation: 1) The new generalized coordinates which are analogous with mean anomaly, right ascension of the ascending node, and argument of perigee, increment linearly with time, and 2) Perturbations due to the Earth's geopotential are already embedded in a given torus to an arbitrary geopotential order. This study examines methods to describe perturbed satellite motion near a reference KAM Torus. The perturbations addressed in this thesis are atmospheric air drag and third-body effects from the Moon.

Perturbed motion was integrated and compared against the unperturbed reference torus motion. For a sample orbit, expressions were numerically derived that allow the modification of the reference torus to allow prediction of the perturbed motion due to drag. It was shown that in the case of third-body lunar effects, the differences between perturbed motion and the reference torus motion cannot be generalized. Instead, there seems to be both evidence and motivation behind attempting to embed the lunar dynamics in the construction of Earth satellite KAM Tori.

To my parents for raising me to appreciate knowledge, hard work, and relaxation.

Acknowledgements

Above all I would like to thank my wife for her unwavering support and understanding. She has sacrificed just as much or more than I have during this journey.

I'd also like to thank my thesis advisor, Dr. Wiesel, for his guidance and patience. I hope that I've memorized at least a small number of his stories so that I can use them in my future academic career.

Luke J. Hagen

Table of Contents

List of Figures

x

List of Tables

List of Acronyms

Acronym

2BP	two-body problem
AP	argument of perigee
ATCFT	analytical form of the truncated, continuous, Fourier transform
CSSI	Center for Space Standards and Innovation
DU	distance units
ECEF	earth-centered-earth-fixed
ECI	earth-centered-inertial
GPS	Global Positioning System
GRACE	Gravity Recovery and Climate Experiment
ISS	International Space Station
KAM	Kolmogorov, Arnold, and Moser
LVLH	local-vertical-local-horizontal
NASA	National Aeronautics and Astronautics Administration
PTE	partial torus extraction
R&A	Regan and Anandakrishnan
RAAN	right ascension of the ascending node
SGP4	simplified general perturbations 4
TU	time units

Nomenclature

A third-body and satellite parameter, $A = \mathbf{P} \cdot \mathbf{e}_3$

a semi-major axis

a_3 semi-major axis of third-body

a_D acceleration due to air drag

a_h acceleration in horizontal direction in LVLH coordinate frame

a_n acceleration in normal direction in LVLH coordinate frame

$\mathbf{a}_{sat/moon}$ acceleration vector of satellite due to Moon

a_V acceleration in velocity direction in LVLH coordinate frame

B third-body and satellite parameter, $B = \mathbf{Q} \cdot \mathbf{e}_3$

B^* ballistic coefficient

C_{nm} gravity coefficient

e eccentricity

$\mathbf{e}_3$ unit vector pointing to third-body

F_g force of gravity

$\mathbf{F}$ force vector

G gravitational constant

H scale height

i 1) inclination; 2) summation index

i_3 inclination of the third-body

$\mathbf{j}$ Fourier series vector summation index

J_2 Earth's second dynamic form factor (oblateness)

M	1) mean anomaly; 2) mass of central body
m	1) mass of satellite; 2) order of associated Legendre polynomial
n	1) mean motion; 2) degree of associated Legendre polynomial
n_3	mean motion of third-body
$\dot{\mathbf{P}}$	torus momenta derivatives vector, $[\dot{P}_1, \dot{P}_2, \dot{P}_3]^T$
$\mathbf{P}$	1) satellite parameter, function of i, Ω, and ω; 2) torus momenta vector, $[P_1, P_2, P_3]^T$
$\mathbf{p}$	physical momenta vector, $[p_1, p_2, p_3]^T$
p	semi-latus rectum
$\dot{P}_1$	torus momentum P_1 time rate of change
P_1	torus momentum
p_1	physical momentum
$\dot{P}_2$	torus momentum P_2 time rate of change
P_2	torus momentum
p_2	physical momentum
$\dot{P}_3$	torus momentum P_3 time rate of change
P_3	torus momentum
p_3	physical momentum
p_i	ith physical momentum
P_n^m	associated Legendre polynomial of order m and degree n
$\dot{\mathbf{q}}$	physical coordinate derivatives vector, $[\dot{q}_1, \dot{q}_2, \dot{q}_3]^T$
$\mathbf{Q}$	1) satellite parameter, function of i, Ω, and ω; 2) torus coordinate vector, $[Q_1, Q_2, Q_3]^T$

$\mathbf{q}$	physical coordinate vector, $[q_1, q_2, q_3]^T$
$\mathbf{Q}_0$	initial torus coordinate vector, $[Q_{01}, Q_{02}, Q_{03}]^T$
$\dot{Q}_1$	torus coordinate Q_1 time rate of change
Q_1	torus coordinate
q_1	physical coordinate
$\dot{Q}_2$	torus coordinate Q_2 time rate of change
Q_2	torus coordinate
q_2	physical coordinate
$\dot{Q}_3$	torus coordinate Q_3 time rate of change
Q_3	torus coordinate
q_3	physical coordinate
q_i	ith physical coordinate
$\mathbf{q}_{int}$	physical coordinate vector of perturbed, integrated motion
$\mathbf{q}_{torus}$	physical coordinate vector of reference torus state
$\mathbf{r}$	position vector
r	position vector magnitude
r_0	reference postion vector magnitude
R_3	potential function due to third-body dynamics
r_3	third-body position vector magnitude
$\mathbf{r}_3$	third-body postion vector
R_e	radius of Earth
r_{error}	position error magnitude between reference torus and perturbed motion states

r_{moon}	magnitude of Moon's position vector
$\mathbf{r}_{moon}$	Moon's position vector
$\mathbf{r}_{sat}$	position vector of satellite
r_{sat}	magntitude of position vector of satellite
$r_{sat/moon}$	magntitude of position vector from satellite to Moon
$\mathbf{r}_{sat/moon}$	position vector from satellite to Moon
S	angle between satellite and third-body position vectors
S_{nm}	gravity coefficient
t	time
u_3	argument of latitude of third-body
$\mathbf{V}$	velocity vector, $[V_x, V_y, V_z]^T$
V	velocity vector magnitude
V_{error}	velocity error magnitude between reference torus and perturbed motion states
V_x	velocity of x coordinate
V_y	velocity of y coordinate
V_z	velocity of z coordinate
$\dot{x}$	physical coordinate velocity
$\mathbf{X}$	physical state vector
x	physical coordinate
$\dot{\mathbf{X}}_{int}$	perturbed, integrated state derivative in physical state variables
$\dot{\mathbf{X}}_{torus}$	reference torus state derivative in physical state variables

$\mathbf{X}_{int}$ perturbed, integrated state in physical state variables

$\mathbf{X}_{torus}$ reference torus state transformed into physical state variables

$\dot{y}$ physical coordinate velocity

$\mathbf{Y}$ canonical state vector; torus state vector

y physical coordinate

$\dot{\mathbf{Y}}_{int}$ perturbed, integrated state derivative transformed into torus state variables

$\dot{\mathbf{Y}}_{torus}$ reference torus state derivative transformed into torus state variables

$\mathbf{Y}_{int}$ perturbed, integrated state transformed into torus state variables

$\mathbf{Y}_{torus}$ reference torus state in torus state variables

$\dot{z}$ physical coordinate velocity

$\mathbf{Z}$ classical orbital element state vector

z physical coordinate

$\boldsymbol{\mathcal{C}}_j$ Fourier series vector coefficient

Δt time difference

$\delta\boldsymbol{\Phi}$ difference phase vector added to phase vector to most closely align reference torus and perturbed motion coordinates

$\delta\Phi_{Q1}$ phase difference added to ϕ_{Q1} to most closely align reference torus and perturbed motion

$\delta\Phi_{Q2}$ phase difference added to ϕ_{Q2} phase vector to most closely align reference torus and perturbed motion

$\delta\Phi_{Q3}$ phase difference added to ϕ_{Q3} phase vector to most closely align reference torus and perturbed motion

$\delta\mathbf{P}_{intercept}$	linear least squares intercept for $\delta\mathbf{P}$
$\delta\mathbf{P}_{slope}$	linear least squares slope for $\delta\mathbf{P}$
$\delta\mathbf{P}$	torus momenta difference vector between reference torus and perturbed motion
$\delta\mathbf{p}$	physical momenta difference vector between reference torus and perturbed motion
$\delta\dot{\mathbf{Q}}_{intercept}$	linear least squares intercept for $\delta\dot{\mathbf{Q}}$
$\delta\dot{\mathbf{Q}}_{slope}$	linear least squares slope for $\delta\dot{\mathbf{Q}}$
$\delta\mathbf{Q}$	torus coordinates difference vector between reference torus and perturbed motion
$\delta\mathbf{q}$	physical coordinates difference vector between reference torus and perturbed motion
δV_x	difference in x coordinate velocity, between reference torus and perturbed motion states
δV_y	difference in y coordinate velocity, between reference torus and perturbed motion states
δV_z	difference in z coordinate velocity, between reference torus and perturbed motion states
δx	difference in x coordinate, between reference torus and perturbed motion states
$\delta\dot{\mathbf{X}}$	physical state derivative difference vector between reference torus and perturbed motion
$\delta\mathbf{X}$	physical state difference vector between reference torus and perturbed motion

δy	difference in y coordinate, between reference torus and perturbed motion states
$\delta \dot{\mathbf{Y}}$	torus state derivative difference vector between reference torus and perturbed motion
$\delta \mathbf{Y}$	torus state difference vector between reference torus and perturbed motion
δz	difference in z coordinate, between reference torus and perturbed motion states
$\mathcal{H}$	hamiltonian
$\mathcal{L}$	lagrangian
μ	gravitational parameter
μ_3	gravitational parameter of third-body
μ_{moon}	gravitational parameter of Moon
$\mathcal{P}$	period
$\mathbf{\Phi}$	phase vector required to most closely align reference torus and perturbed motion coordinates
ϕ	spherical coordinate, azimuth
$\mathbf{\Phi}_{intercept}$	linear least squares intercept for $\mathbf{\Phi}$
Φ_{Q1}	phase required to most closely align reference torus and perturbed motion Q_1
Φ_{Q2}	phase required to most closely align reference torus and perturbed motion Q_2
Φ_{Q3}	phase required to most closely align reference torus and perturbed motion Q_3

$\mathbf{\Phi}_{slope}$	linear least squares slope for $\mathbf{\Phi}$
ρ	atmospheric density
ρ_0	atmospheric density at reference heigh
$\mathcal{S}_j$	Fourier series vector coefficient
$\mathcal{T}$	kinetic energy per unit mass
θ	spherical coordinate, inclination
$\mathcal{V}$	potential function
ν	true anomaly
Ω	right ascension of the ascending node
ω	argument of perigee
ω_1	torus coordinate Q_1 basis frequency
ω_2	torus coordinate Q_2 basis frequency
Ω_3	right ascension of the ascending node of the third-body
ω_3	torus coordinate Q_3 basis frequency
$\omega_\oplus$	Earth's rotational angular velocity magnitude
$\boldsymbol{\omega}_\oplus$	Earth's rotational angular velocity vector, $[0, 0, \omega_\oplus]^T$
ω_{ls-est}	estimated frequency of lunar system
ω_{ls}	frequency of lunar system
ω_{moon}	orbital angular velocity of the Moon
$\boldsymbol{\omega}$	torus basis frequency vector

Effects of Air Drag and Lunar Third-Body Pertubrations on Orbital Motion Near a Reference KAM Torus

I. Introduction

Though ancient peoples have been watching the nighttime sky for millennia, the study of orbital mechanics as we know it began with such giants as Nicholas Copernicus, Johannes Kepler, and Galileo Galilei in the 17th century. These great thinkers were simply trying to reconcile the motion of the heavens with rudimentary thoughts such as the earth being flat and the center of the known universe. Their observations reasonably focused on heavenly bodies such as the Sun, Moon, and planets.

Flip a few pages forward in the calendar to the twentieth century, and humanity can be found leveraging orbital mechanics for amazing applications. The Soviet Union placed the first artificial satellite in orbit around the Earth in 1957. The United States of America landed men on the moon in 1969. Again, fast forward in time, but now to the current day. The nations of the world utilize space both commercially and militarily. Commercial applications include Sun and Earth weather observation, communication, entertainment, and imaging. Military applications include various forms of intelligence gathering, communications, precision navigation and timing, and space situational awareness.

1.1 Motivation

Somewhere in the transition from predicting the motion of heavenly bodies to the placement of artificial satellites in low-earth orbit, it became necessary to consider how classical satellite orbits as defined by Kepler are perturbed by small forces over time. Current day space applications require high accuracy knowledge of a spacecraft's

position as well as the ability to predict the spacecraft's state at some time in the future. Today, this is achieved by collecting observations of position and velocity of the satellite using ground-based sensors. These sensors include optical sensors and the "Space Fence," a very high frequency radar network, all owned and operated by the United States. The observations are combined to produce a description, or state, of the spacecraft's orbit, called orbital elements. The spacecraft's state can then be propagated to some arbitrary time in the future by means of numerical integration.

Unfortunately, as the "space is big" theory for on-orbit disposal of dead satellites, rocket bodies, and junk is disproven by costly collisions. For example, the collision of the Iridium 33 satellite with the defunct Russian Cosmos 2251 satellite in February 2009 was not predicted ahead of time. The collision was only known to have occurred after Iridium 33 become unresponsive and US space operators began tracking a debris cloud which originated at Iridium 33's previous position. While the two satellites were flagged by the Center for Space Standards and Innovation (CSSI) as having a close approach of just over half of a kilometer, there were other closer approaches predicted that day (4).

The problem of identifying probable collisions with sufficient lead-time and accuracy cannot be solved with today's methods. Enter the KAM Theorem. First proposed by Andrey Kolmogorov in 1954, and later extended and proved by Vladimir Arnold in 1963 and Jürgen Moser in 1962, the KAM Theorem potentially offers a new method of attacking this problem. The KAM Theorem, when applied to Earth orbiting satellites, essentially transforms the physical variable state description of the system to KAM Torus variables in which three coordinates increment linearly with time and three momenta remain constant. The KAM Torus can be visualized as a multi-dimensional donut on which the satellite traverses the surface. The KAM Theorem may also provide a replacement to the current-day two-line element sets now used

to publish a satellite's ephemerides which are subsequently used in many applications including satellite collision predictions. The replacement is only now possible due to today's computing power combined with the new application of the KAM Theorem and its ability to consider the entire Earth's geopotential not as a perturbation, but as a fundamental component of the orbit description.

The study of orbital perturbations follows one of two approaches: general perturbations and special perturbations. General perturbation theory is mainly analytical and seeks to understand how on average various perturbations affect a satellite's orbital elements. General perturbation theory will offer understanding to the orbital mechanist, but not the precision knowledge required for today's applications or for predicting and preventing satellite collisions. Special perturbation theory well reflects its name – it involves numerically integrating the equations of motion to determine the specific solution of a certain satellite and its initial conditions. Change the initial conditions and the numerical integration will have to be re-performed for a new, unique solution. Considering the incredible number of artificial satellites orbiting the Earth, the special perturbations approach to predicting and preventing satellite collisions is inefficient if not impossible. In the search for new methods KAM Theory may provide the answer.

As more nations around the world gain homegrown access to space, the number of artificial satellites purposefully put into space to orbit the Earth will increase dramatically. But along with the purposeful increase will come the passive increase. As the satellite count increases, so too does the probability for collisions. As an illustration, ponder this message from T.S. Kelso, posted on Twitter on January 4, 2011 (10): "*TLE data released for 76 more pieces of Cosmos 2251 debris, bringing total to 1,423 with only 75 pieces having decayed.*" In less than two years, 1,348 known pieces of debris from the Iridium and Cosmos collision remain. Not considering the debris

3

yet to be identified, these 1,348 pieces must be tracked; however, just because debris is tracked does not mean it cannot or will not collide with other satellites in the future.

1.2 Approach

In this work, the author has attempted to quantify how air drag and third-body lunar perturbations affect orbital motion near a reference KAM Torus. Expressions for the average effects to the torus coordinates and momenta were determined. The satellite's perturbed state was numerically integrated and transformed into torus coordinates and momenta for comparison to the nearby reference torus. A simple atmosphere model was utilized for drag calculations. The perturbing accelerations due to air drag and lunar third-body were incorporated in the numerical integration. For simplicity, the moon was assumed to orbit in the equatorial plane.

1.3 Problem Statement

Since the KAM Theorem is based on a nearly integrable Hamiltonian system, it is necessary to show that application of the theorem to low-earth orbiting satellites is not precluded by air drag, which is a non-conservative force, or lunar-third body effects. The deviation of the perturbed motion from the reference torus should be quantified and understood. If the deviation is non-negligible, a method should be proposed for accounting for these perturbing effects.

II. Background

The simple case of an object orbiting a larger body is described as a central force problem in which the force is due to gravity. For a central force problem

$$\mathbf{F} = F_g \frac{\mathbf{r}}{r} \tag{1}$$

where F_g is defined in Equation 2 and $\frac{\mathbf{r}}{r}$ is the unit position vector:

$$F_g = -\frac{GMm}{r^2} \tag{2}$$

where G is the gravitational constant, M is the mass of the larger body, and m is the mass of the smaller body.

This version of the central-force problem is often referred to as the "Keplerian" problem and results in the familiar orbital solutions in which the state of an orbiting mass is known for all time. Especially in satellites orbiting the Earth, it can be readily seen that reality quickly diverges from the Keplerian solution.

2.1 Perturbations to the Keplerian Problem

Over the years, orbital mechanists have shown that many forces perturb the solutions predicted by the two-body problem. Earth orbiting satellites are subject to the gravitational potential differences of the non-spherical Earth. Spacecraft orbiting the Earth at low altitudes are susceptible to force resulting from air drag. Third-body effects from the Moon also perturb the Keplerian solution. Other sources of perturbation include the Sun's gravity and solar radiation pressure, but these will not be discussed in this work.

2.1.1 Geopotential. The assumption of a "point-mass" is made in the deriva-
tion of Keplerian motion. For accurate applications, the point-mass assumption cannot
be made as the Earth is not perfectly spherical. The shape of the Earth is actually
that of a spheroid – the shape that is obtained by rotating an ellipse about one
of its axes. This mass distribution results in a gravity potential function that can be
described using zonal, sectorial, and tesseral harmonics. Zonal harmonics are indepen-
dent of longitude and include the famous oblateness term, "J_2." Sectorial harmonics
are independent of latitude and resemble orange slices. Finally, tesseral harmonics are
dependent on both longitude and latitude and resemble a chessboard placed over the
surface of the Earth (7).

The Earth's geopotential function is given by Wiesel (23) as

$$\mathcal{V}(r, \theta, \phi) = -\frac{\mu}{r} \sum_{n=0}^{\infty} \sum_{m=0}^{n} \left(\frac{r}{R_e}\right)^{-n} P_n^m (\cos \theta) (C_{nm} \cos m\phi + S_{nm} \sin m\phi) \qquad (3)$$

where r, θ, and ϕ are spherical coordinates; R_e is the radius of the Earth; μ is the
Earths gravitational parameter; C_{nm} and S_{nm} are constants specifying the shape of the
gravitational field; and P_n^m are associated Legendre polynomials. When $m = n = 0$,
the geopotential function degenerates into the Keplerian potential given by

$$\mathcal{V}(r) = -\frac{\mu}{r} \qquad (4)$$

Ideally, one could use the entire geopotential to derive the perturbations to the
Keplerian motion of a satellite. Unfortunately, developing the perturbations analyt-
ically for just the second zonal harmonic ($m = 0, n = 2$) is very complex. On the
other hand, since the second zonal harmonic is by far the largest contributor to non-
Keplerian effects, these perturbations to the Keplerian solution can be isolated and

well understood. The average rate of change of the orbital elements due to the second zonal harmonic will not be derived here but are listed by Schaub (16):

$$\frac{da}{dt} = 0 \tag{5}$$

$$\frac{de}{dt} = 0 \tag{6}$$

$$\frac{di}{dt} = 0 \tag{7}$$

$$\frac{d\Omega}{dt} = -\frac{3}{2}J_2 n \left(\frac{R_e}{p}\right)^2 \cos i \tag{8}$$

$$\frac{d\omega}{dt} = \frac{3}{4}J_2 n \left(\frac{R_e}{p}\right)^2 \left(5\cos^2 i - 1\right) \tag{9}$$

$$\frac{dM}{dt} = \frac{3}{4}J_2 n \left(\frac{R_e}{p}\right)^2 \sqrt{1 - e^2} \left(3\cos^2 i - 1\right) \tag{10}$$

where a is the semi-major axis, e is the eccentricity, i is the inclination, Ω is the right ascension of the ascending node (RAAN), J_2 is a constant, n is the mean motion, R_e is the radius of the Earth, p is the semi-latus rectum, ω is the argument of perigee (AP), and M is the mean anomaly. Note that Equations 5, 6, 7, 8, 9, and 10 are the secular rates and do not exhibit short or long period oscillations.

2.1.2 Air Drag Perturbations.   The Earth's atmosphere extends to approximately 1500 km altitude. Satellites orbiting in the regime below 1000 km altitude are subject to a non-negligible force due to air drag that is a function of cross-sectional area, mass, drag coefficient, velocity, and air density (6). Because drag is a non-conservative force, the satellite will continuously lose energy when exposed to the drag force. Elliptical orbits will circularize as the apogee altitude is continuously reduced due to the energy loss. Once the orbit has been circularized, the net effect is a

reduction of orbital altitude until the satellite's velocity is reduced to the point that it cannot stay in orbit.

2.1.2.1 Effects of Air Drag on Orbital Elements. Schaub describes (16) inserting the acceleration due to air drag into Gauss' variational equations to arrive at average rates of change to the classical orbital elements. Gauss variational equations are listed below:

$$\frac{da}{dt} = \frac{2a^2V}{\mu} a_V \tag{11}$$

$$\frac{de}{dt} = \frac{1}{V} \left(\frac{r}{a} \sin \nu \, a_n + 2 \left(e + \cos \nu \right) a_V \right) \tag{12}$$

$$\frac{di}{dt} = \frac{r \cos \left(\omega + \nu \right)}{\sqrt{\mu a \left(1 - e^2 \right)}} a_h \tag{13}$$

$$\frac{d\Omega}{dt} = \frac{r \sin \left(\omega + \nu \right)}{\sin i \sqrt{\mu a \left(1 - e^2 \right)}} \tag{14}$$

$$\frac{d\omega}{dt} = \frac{1}{eV} \left(-a_n \left(2e + \frac{r}{a} \right) \cos \nu + 2 a_V \sin \nu \right) - \frac{r \sin \left(\omega + \nu \right) \cos i}{\sqrt{\mu a \left(1 - e^2 \right)}} a_h \tag{15}$$

$$\frac{dM}{dt} = n + \frac{\sqrt{1 - e^2}}{eV} \left(\frac{r}{a} a_n \cos \nu - 2 \left(1 + \frac{e^2 r}{a \left(1 - e^2 \right)} \right) a_V \sin \nu \right) \tag{16}$$

where V is the velocity; a_V, a_h, and a_n are the accelerations in the local-vertical-local-horizontal (LVLH) coordinate frame; μ is the Earth's gravitational parameter; r is the radius; and ν is the true anomaly.

Air drag only occurs in the velocity direction, $a_h = 0$ and $a_n = 0$, leaving only $a_V = a_D = -V^2/2B^*\rho$ which when placed in the variational equations yields (16):

$$\frac{da}{dt} = -B^* \rho \frac{V^3}{a_n^2} \tag{17}$$

$$\frac{de}{dt} = -B^* \rho V \left(e + \cos \nu \right) \tag{18}$$

8

$$\frac{di}{dt} = 0 \tag{19}$$

$$\frac{d\Omega}{dt} = 0 \tag{20}$$

$$\frac{d\omega}{dt} = -B^* \rho V \frac{\sin \nu}{e} \tag{21}$$

$$\frac{dM}{dt} = n + B^* \rho V \frac{\sqrt{1-e^2}}{e} \left(1 + e^2 \frac{r}{a\left(1-e^2\right)} \right) \sin \nu \tag{22}$$

where B^* is the ballistic drag coefficient and ρ is the atmospheric density at altitude. These equations give us insight into the effect of drag on a satellites orbit. Quite obviously, the semi-major axis will shrink but the other effects really require the parameters to be evaluated as an orbit is propagated to gain understanding.

Note that as eccentricity approaches a zero value, these equations are invalid since the argument of perigee and right ascension of the ascending note are undefined. The eccentricity in the denominator of two of the equations would present a problem as well.

2.1.2.2   Atmosphere Model.   The properties of the atmosphere are diverse by location and time. A simplistic model that only considers variation by altitude is the exponential model in which the density of the atmosphere is simply a function of a reference density and height:

$$\rho(r) = \rho_0 e^{\frac{-(r-r_0)}{H}} \tag{23}$$

where ρ_0 is the reference density at some reference position, r_0, and H is the scale height.

For the purposes of this research, a more realistic model must be considered because above 86 km altitude, the atmosphere is highly dynamic (15). The model chosen

9

for this research is detailed by Regan and Anandakrishnan (R&A). The atmosphere is considered to be broken into layers of atmospheric strata. The boundary between each stratum is considered to occur when the atmosphere is isothermal. R&A provide a TRUEBASIC algorithm that calculates the atmospheric properties of temperature, pressure, and density, for a given altitude. The R&A Standard Atmosphere is a hybrid model in which the U.S. 1976 Standard Atmosphere is used for altitudes from 0 to 86 km and the U.S. 1962 Standard Atmosphere is used for altitudes above 86 km. R&A created this hybrid model for sake of algorithm simplicity. Above 86 km, the 1976 model contains two strata in which the lapse rates are not linear but rather elliptical and exponential. R&A make the argument that while these rates could be calculated, their minor difference from the 1962 model are easily overcome by error introduced by incoming solar radiation.

The author has translated the R&A Standard Atmosphere TRUEBASIC algorithm into C++ for compatibility with Wiesel's software (21). The translated algorithm provides only density as it is the only output required for this research. Figure 1 shows the density of the atmosphere from 0 to 700 km per the adapted R&A algorithm.

The algorithm was validated by comparing its output to the altitude/density profile of the U.S. 1962 & 1976 Standard Atmospheres published by National Aeronautics and Astronautics Administration (NASA). Figure 2 shows the 1962 & 1976 U.S. Standard Atmosphere and three earlier U.S. Standard and model atmospheres.

Even more advanced models must consider many additional factors including: longitude and latitude, time of day, time of the year, solar cycle, and solar storms. For the purposes of this research, models beyond the complexity of the chosen model will not be utilized since the intent is to understand how air drag modifies the KAM Torus
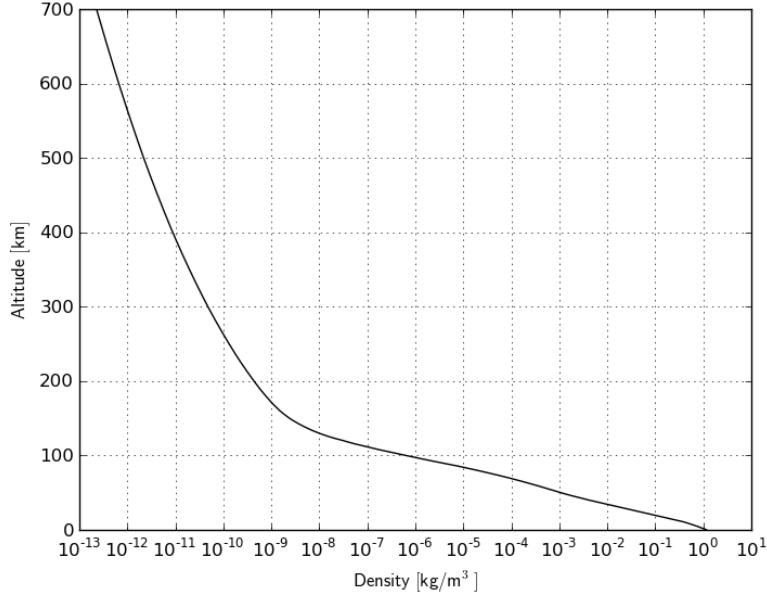
Figure 1: Atmospheric Density Plot Generated From Translated R&A Standard Atmosphere Algorithm

coordinates and momenta in general, rather than provide precise state predictions in a specific scenario.

2.1.3 Moon Perturbations. The third-body problem has been treated by numerous distinguished orbital mechanists (3), such as L. Euler, C. E. DeLaunay, H. Poincaré, G. W. Hill, and E. W. Brown as well as D. Brouwer (3), D. Vallado (17), Schaub (16), Chao (6) and many more. Due to its difficulty, the most insightful results have been garnered when the three bodies are restricted to in plane motion.

Chao (6) writes that the disturbing function for third-body motion is given as

$$R_3 = \frac{\mu_3}{r_3} \left[\left(1 + \frac{r^2}{r_3^2} - \frac{2r}{r_3} \cos S \right)^{-\frac{1}{2}} - \frac{r \cos S}{r_3} \right] \tag{24}$$

11
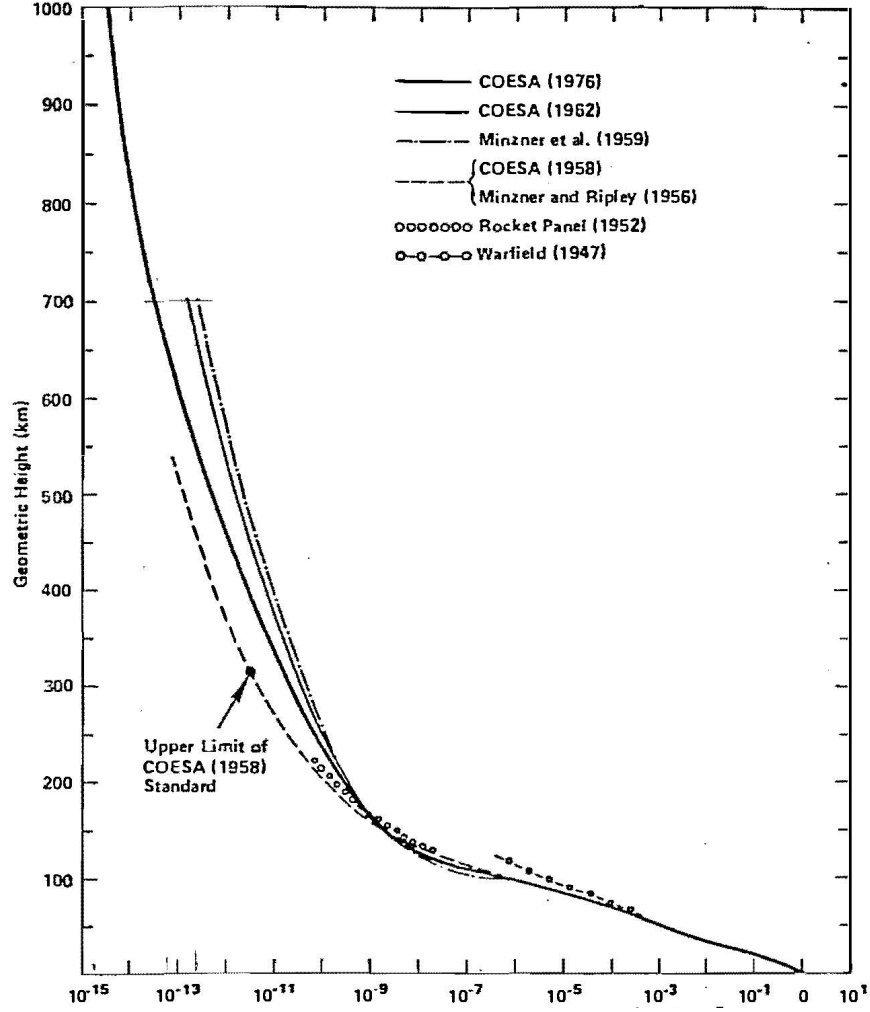
Figure 2: 1962 & 1976 U.S. Standard Atmosphere (14)

where μ_3 is the gravitational constant of the third-body, r_3 is the position vector magnitude of the third-body, r is the position vector magnitude of the satellite, and S is the angle between the two position vectors $\mathbf{r}$ and $\mathbf{r}_3$.

Kaufman (9) showed that when $r/r_3 << 1$, the square-root term in Equation 24 can be expanded with higher order terms discarded. Kaufman then applied the method of averaging to remove the short period terms, resulting in a new expression for the disturbing function:

12

$$R_3 = \frac{a^2 n_3^2}{2} \left(\frac{a_3}{r_3}\right)^3 \left\{ \left[\frac{3}{2}\left(A^2 + B^2\right) - 1\right]\left(1 + \frac{3e^2}{2}\right) + \frac{3}{2}\left(A^2 - B^2\right)\frac{5e^2}{2} \right\} \qquad (25)$$

where $A = \mathbf{P} \cdot \mathbf{e}_3$ and $B = \mathbf{Q} \cdot \mathbf{e}_3$; a is the semi-major axis and e is the eccentricity of the satellite; a_3 is the semi-major axis of the third-body, r_3 is the position vector magnitude of the third-body, and n_3 is the mean motion of the third body; and

$$\mathbf{P} = \begin{bmatrix} \cos\Omega\cos\omega - \sin\Omega\sin\omega\cos i \\ \sin\Omega\cos\omega + \cos\Omega\sin\omega\cos i \\ \sin\omega\sin i \end{bmatrix} \qquad (26)$$

$$\mathbf{Q} = \begin{bmatrix} -\cos\Omega\sin\omega - \sin\Omega\cos\omega\cos i \\ -\sin\Omega\sin\omega + \cos\Omega\cos\omega\cos i \\ \cos\omega\sin i \end{bmatrix} \qquad (27)$$

$$\mathbf{e}_3 = \begin{bmatrix} \cos\Omega_3\cos u_3 - \sin\Omega_3\sin u_3\cos i_3 \\ \sin\Omega_3\cos u_3 + \cos\Omega_3\sin u_3\cos i_3 \\ \sin u_3\sin i_3 \end{bmatrix} \qquad (28)$$

where $\mathbf{e}_3$ is the unit postion vector of the third-body, i_3 is the inclination of third-body, u_3 is the argument of latitude of the third-body, and Ω_3 is the RAAN of the third-body.

Chao (5) then expanded the disturbing function per the classical orbital elements. The final results (6) are equations for the rate of change of the classical orbital elements of the satellite that are being perturbed by the third-body. The equations are too lengthy to cover here but they are heavily dependent on the AP and RAAN of both the third-body and the satellite. Due to assumptions that will be made to

13

simplify the Moon model for this research – chiefly that the Moon's orbit is circular about the Earths equator (AP and RAAN are undefined) – these equations will not provide results for comparison in this research.

Vallado (17) summarizes the effects on a satellite due to third-body perturbations as periodic for semi-major axis, eccentricity, and inclination and secular and periodic for mean anomaly, RAAN, and AP. An approach utilizing KAM Theory will be discussed in §3.3 – the results will be compared against this summary.

2.2 KAM Theory

The KAM Theorem was developed and proved over the period of about a decade by Andrey Kolmogorov (11), Vladimir Arnold (1), and Jürgen Moser (13). Essentially, the KAM Theorem states that the solutions of a slightly perturbed Hamiltonian system will exist on the surface of a torus.

KAM theory is born out of a special subclass of Hamiltonian dynamics that exhibit periodic motion at certain fundamental frequencies. The consequence of being characterized as a periodic Hamiltonian system is that the physical variables can be transformed into coordinate-momentum pairs in which the momenta are constant and the coordinates are angles that increment linearly with time. This becomes one of the primary benefits of describing an orbital system as a KAM Torus. In current application of the KAM theory to Earth orbiting systems, the transformation results in three system coordinates that increment linearly with time

$$\mathbf{Q} = \mathbf{Q}_0 + \boldsymbol{\omega} t \tag{29}$$

where $\mathbf{Q}$ is the coordinate vector, $\mathbf{Q}_0$ is the initial values of the coordinate vector, and $\boldsymbol{\omega}$ is the basis frequency vector.

14

In addition to the coordinates, three constant momenta, $\mathbf{P}$, result from the transformation to the KAM Torus. Predicting the future state of the system becomes trivial in this scenario. The application of KAM Theory to Earth orbiting systems offers another tempting benefit to the orbital mechanic: the Earth's geopotential is incorporated in the KAM Torus to an arbitrary order, thus converting geopotential perturbations in physical variables into standard torus behavior.

The application of KAM Theory to Earth satellites had remained relatively untouched until Wiesel first argued that at least some Earth orbits can be described by KAM Tori (20). The evidence confirming this argument was first, that the Earth satellite torus contained only three fundamental frequencies as predicted by the Hamilton-Jacobi theorem; and second, that the motion of the satellite could be described via a Fourier series expansion. Wiesel also showed that the two-body problem in the earth-centered-earth-fixed (ECEF) frame and the simplified general perturbations 4 (SGP4) model can be considered to be torus models as well (22). In the same paper, Wiesel also showed that the KAM Torus is an effective perturbation theory for an Earth satellite since the entire Earth geopotential is incorporated in the torus.

Several doctoral and graduate students of Wiesel have also contributed to the body of Earth satellite KAM Tori research. B. Little attempted to fit tori to actual data from the Jason-1 and Gravity Recovery and Climate Experiment (GRACE) satellites (12). He determined that Jason-1 does indeed lie on a torus. On the other hand, he was unable to fit GRACE to a torus and proposed that perturbation due to air drag may have been responsible. C. Craft investigated the applicability of KAM Theory to Earth orbiting satellite formations (8). He determined that formations with large physical separations have proportionally large secular drift which may preclude the use of KAM Theory for formation flight applications. Additionally, he showed that smaller formations in which the satellites have small separations in the torus

15

coordinates result in drift rates easily countered by current-day technology such as electric propulsion. R. Bordner fit tori to Global Positioning System (GPS) satellite orbital data and found that the resonant nature of the GPS orbit resulted in the smallest system frequency being masked by the fact that an entire period did not occur within the orbital data set (2). This trouble led Bordner to develop a new procedure of fitting the frequency clusters within the orbital data to the analytical form of the truncated, continuous, Fourier transform (ATCFT) to form the KAM Torus.

III. Methodology

The overall approach to understanding how motion near a KAM Torus is perturbed by air drag and the moon will be to propagate the perturbed orbit via numerical integration, propagate the non-perturbed torus orbit by updating the torus coordinates as described in §2.2, and then compare the two resulting states in terms of torus coordinates and momenta. These state differentials will then be transformed back to physical coordinates to aid in understanding the type and quantity of error.

Specifically, the remainder of the research will consider and compare three cases:

1. *Baseline*: comparison of unperturbed numerically integrated motion to reference torus motion. Any error between the two should be due to linearizations and numerical truncation

2. *Drag*: comparison of drag perturbed numerically integrated motion to reference torus motion

3. *Lunar*: comparison of third-body lunar perturbed numerically integration motion to reference torus motion

Discussion and figures in the remaining sections of this work will refer to these cases as "Three Cases" or "Baseline, Drag, and Lunar Cases." Wiesel has developed a C++ software package (21), that evaluates the motion of a satellite near a reference torus. The inner workings of the software will be described in §§3.2.1-2. The software was specifically designed to examine the motion of an Earth satellite with initial coordinates and/or momenta offsets from the reference torus. The author has modified this software to evaluate perturbed motion near a reference torus in the following ways:

- Addition of standard atmosphere object for calculating atmospheric density at altitudes 0-700 km

- Calculation of position and velocity error for total or single state differences between perturbed numerically integrated motion and reference torus motion
- Calculation of rates of change of torus coordinates and momenta
- Option to execute software in three additional configurations:
  - Motion perturbed by air drag
  - Motion perturbed by lunar third-body effects
  - Motion perturbed by both air drag and lunar-third body

A specific description of how the software was modified to incorporate perturbing accelerations due to air drag and the Moon's third-body effects is presented in §§3.2.2.2-3.

The author performed data analysis and plot generation using the open source scripting language Python extended by the following open source packages:

- *NumPy* – numerical package that offers n-dimensional array object as well as many numerical functions for operations on arrays
- *SciPy* – scientific package that offers functions for integration, optimization, linear algebra, fourier transforms, etc
- *Matplotlib* – plotting package with functionality similar to common numerical plotting tools

3.1   Obtaining the Reference KAM Torus

3.1.1   Method for Finding the KAM Torus.   While several methods exist for finding the KAM Torus of an Earth orbiting satellite, the following method, established by Wiesel and Bordner (2) was used. First, an orbit with an initial state is chosen and numerically integrated, including only geopotenial perturbations, forward and backward in time for six months in both directions. Next, the raw position data

from the numerical integration of the orbit is transformed into a spectral plot. The spectral plot is then sectioned into groups of frequency lines where the analytical form of the truncated, continuous, Fourier transform (ATCFT) is used to fit the frequency lines and determine the Fourier coefficients (2). Bordner terms this as the "Frequency Cluster-Based Approach."

3.1.2 KAM Tori Utilized in Research. The author utilized two tori in this research. Torus #1's classical orbital element characterization is listed in Table 1. The classical orbital elements were converted to the associated position and velocity vectors and integrated forward and backward in time by 6 months for one year of total data. The torus was then created using the approach developed by Bordner (2) as described in §3.1.1.

The second torus was provided by Yates (24). He obtained high precision orbital data of the International Space Station (ISS). He then passed the data through a Bayes filter several times in order to condition the data such that it was conducive to matching with a KAM Torus. The torus was finally constructed as described in §3.1.1 with the exception that the conditioned ISS orbital data was used in place of the numerical integration data. The classical orbital element characterization of the ISS orbit is listed in Table 1:

Table 1: Classical Orbital Elements of Orbits Represented by Tori

Torus	**a [DU]**	**e**	**i°**	**Ω°**	**ω°**	**M°**
#1	1.1	0.05	30.00	261.7	141.4	88.4
#2 (ISS)	1.05	0.001	51.6	300.2	112.7	322.4

Though two tori were available for analysis, the majority of this work considers only Torus #1 because the results for each torus are very similar. Results are assumed to refer to Torus #1 unless indicated otherwise. Note that both tori have

19

semi-major axes that are within the Earth's atmosphere and will be affected by air drag (important if the effects of air drag on tori are to be analyzed).

3.2 Numerical Integration of Perturbed Motion Near the Reference Torus

3.2.1 Extracting Initial State from the Torus. The initial conditions in physical coordinates must be established from the torus via multiple Fourier series (22):

$$\mathbf{q} = \sum_{\mathbf{j}} \left[\boldsymbol{C_j} \cos\left(\mathbf{j} \cdot \mathbf{Q}\right) + \boldsymbol{S_j} \sin\left(\mathbf{j} \cdot \mathbf{Q}\right) \right] \tag{30}$$

where $\boldsymbol{C_j}$ and $\boldsymbol{S_j}$ are vector coefficients with a vector summation index $\mathbf{j}$, and $\mathbf{Q}$ are the torus coordinates. Next, the initial momenta must be determined through manipulation of the Lagrangian:

$$\mathbf{p} = \frac{\partial \mathcal{L}}{\partial \dot{\mathbf{q}}} \tag{31}$$

where $\mathbf{p}$ are the physical momenta, $\mathcal{L}$ is the Lagrangian, and $\dot{\mathbf{q}}$ are the inertial time derivatives of the physical coordinates.

3.2.2 Equations of Motion. The equations of motion will be addressed in three parts. The primary effort considers the two-body problem perturbed by the geopotential. Once this effort is properly posed, it will be extended to air drag and Moon third-body motion perturbations.

3.2.2.1 Keplerian Motion Plus Geopotential. In the Cartesian space rotating with the Earth, the ECEF coordinate system, the Hamiltonian for an orbiting satellite is derived as any other Hamiltonian, beginning with Equation 32.

$$\mathcal{H} = \sum_i p_i \dot{q}_i - \mathcal{L} \tag{32}$$

where p_i are momenta, $\dot{q}_i$ are the coordinate velocities, $\mathcal{L}$ is the Lagrangian, and $\mathcal{H}$ is the Hamiltonian.

The Lagrangian is calculated by subtracting a system's potential energy from a term representing the system's kinetic energy as represented by Equation 33.

$$\mathcal{L} = \mathcal{T} - \mathcal{V} \tag{33}$$

where $\mathcal{T}$ is the kinetic energy term and $\mathcal{V}$ is the potential energy term.

The energy term can easily be calculated via Equation 36. Start with the satellite's position expressed in coordinates x, y, and z in the ECEF frame. The inertial derivative of the position can be obtained with the help of the Transport Theorem and is shown by Equation 34:

$$\dot{\mathbf{r}} = {}^{ECI}_i\dot{\mathbf{r}} = {}^{ECEF}_i\dot{\mathbf{r}} + \boldsymbol{\omega}_\oplus \times \mathbf{r} \tag{34}$$

which when expanded yields

$$\dot{\mathbf{r}} = \mathbf{V} = \begin{bmatrix} \dot{x} - y\omega_\oplus \\ \dot{y} + x\omega_\oplus \\ \dot{z} \end{bmatrix} = \begin{bmatrix} \dot{q}_1 \\ \dot{q}_2 \\ \dot{q}_3 \end{bmatrix} \tag{35}$$

Next, now that the velocity is known in terms of the coordinates, the kinetic energy per unit mass can be calculated:

$$\mathcal{T} = \frac{1}{2}V^2 = \frac{1}{2}\left[(\dot{x} - y\omega_\oplus)^2 + (\dot{y} + x\omega_\oplus)^2 + \dot{z}^2\right] \tag{36}$$

Now the Lagrangian becomes

$$\mathcal{L} = \frac{1}{2}\left[(\dot{x} - y\omega_\oplus)^2 + (\dot{y} + x\omega_\oplus)^2 + \dot{z}^2\right] - \mathcal{V}(x, y, z) \tag{37}$$

Next, to calculate the momenta, Equation (34) is utilized:

$$\mathbf{p} = \frac{\partial \mathcal{L}}{\partial \dot{\mathbf{q}}} \tag{38}$$

The momenta are

$$\mathbf{p} = \begin{bmatrix} \dot{x} - y\omega_\oplus \\ \dot{y} + x\omega_\oplus \\ \dot{z} \end{bmatrix} \tag{39}$$

For use in calculation of the Hamiltonian, Equation 39 is rearranged to solve for the rate of change of the coordinates:

$$\dot{\mathbf{q}} = \begin{bmatrix} p_1 - y\omega_\oplus \\ p_2 + x\omega_\oplus \\ p_3 \end{bmatrix} \tag{40}$$

where p_1, p_2, and p_3 are the physical momenta.

Now utilizing Equations 32, 37, 39, and 40 the Hamiltonian is found to be

$$\mathcal{H} = \frac{1}{2}\left(p_1^2 + p_2^2 + p_3^2\right) + \omega_\oplus y p_1 - \omega_\oplus x p_2 + \mathcal{V} \tag{41}$$

where $\mathcal{H}$ is the Hamiltonian, x, y, and z are the coordinates, $\omega_\oplus$ is the Earth's angular velocity, and $\mathcal{V}$ is the Earth's geopotential as described in Equation 3.

The coordinates and momenta are the system state:

$$\mathbf{X} = \begin{bmatrix} q_1 \\ q_2 \\ q_3 \\ p_1 \\ p_2 \\ p_3 \end{bmatrix} = \begin{bmatrix} x \\ y \\ z \\ V_x \\ V_y \\ V_z \end{bmatrix} \tag{42}$$

where q_1, q_2, and q_3 are the physical coordinates and V_x, V_y, and V_z are the physical coordinate velocities.

Since the ECEF coordinate system is being used, the Earth's gravitational potential, $\mathcal{V}$, is not a function of time but of only the satellite's position. Therefore, Hamilton's equations can easily be used to determine the time rate of change of the coordinates and momenta:

$$\dot{q}_i = \frac{\partial \mathcal{H}}{\partial p_i} \tag{43}$$

$$\dot{p}_i = -\frac{\partial \mathcal{H}}{\partial q_i} \tag{44}$$

Because the coordinates are the position and the momenta are the velocity, Equations 43 and 44 can be used to determine how position and velocity of the Earth satellite are changing with time:

$$\dot{x} = \frac{\partial \mathcal{H}}{\partial V_x} = V_x + \omega_\oplus y \tag{45}$$

$$\dot{y} = \frac{\partial \mathcal{H}}{\partial V_y} = V_y - \omega_\oplus x \tag{46}$$

23

$$\dot{z} = \frac{\partial \mathcal{H}}{\partial V_z} = V_z \tag{47}$$

$$\dot{V}_x = -\frac{\partial \mathcal{H}}{\partial x} = \omega_\oplus V_y - \frac{\partial \mathcal{V}}{\partial x} \tag{48}$$

$$\dot{V}_y = -\frac{\partial \mathcal{H}}{\partial y} = -\omega_\oplus V_x - \frac{\partial \mathcal{V}}{\partial y} \tag{49}$$

$$\dot{V}_z = -\frac{\partial \mathcal{H}}{\partial z} = -\frac{\partial \mathcal{V}}{\partial z} \tag{50}$$

Note that while these equations of motion were derived with the Hamiltonian (i.e. conservative system), accelerations due to non-conservative forces or additional conservative forces can be added to $\dot{V}_x$, $\dot{V}_y$, and $\dot{V}_z$ with ease. This approach will be taken in §§3.2.2.2-3 when specifically addressing air drag and the third-body Moon problem.

Now that the equations of motion are established, numerical integration can be performed. The Hamming fourth order predictor/corrector numerical integrator was utilized. While the equations of motion only contain accelerations due to conservative forces, the accuracy of the numerical integration can be checked by evaluating the Hamiltonian at each time step. Once air drag or lunar effects are added this check will not be valid.

3.2.2.2 Air Drag. The incorporation of air drag in the equations of motion is as simple as modifying Equations 48, 49, and 50 to include the following vector term:

24

$$\dot{\mathbf{V}} = -\frac{1}{2}\rho V^2 \frac{\mathbf{V}}{V} B^* = -\frac{1}{2}\rho V \mathbf{V} B^* \qquad (51)$$

where ρ is the density of the atmosphere, V is the velocity of the satellite relative to the atmosphere, $\mathbf{V}$ is the velocity vector in the ECEF frame, and B^* is the ballistic coefficient.

The ballistic coefficient is dependent on the drag coefficient, cross-sectional area in the velocity direction, as well as the mass. Note that the dimensions of the ballistic coefficient must be area per mass for Equation 51 to be valid. Many Earth orbiting satellites have rotational motion about their center of mass, which results in the values of the drag coefficient and cross-sectional area varying with time. For the purposes of this research, the ballistic coefficient will be assumed to be constant. Table 2 summarizes ballistic coefficients for several satellites:

Table 2: Ballistic Coefficients of Various Satellites (18)

Satellite	Shape	Max. Ballistic Coef. [kg/m²]	Min. Ballistic Coef. [kg/m²]	Max. Ballistic Coef. [m²/kg]	Min. Ballastic Coef. [m²/kg]
Oscar-1	Box	42.8	16.7	0.0234	0.0599
Intercos.-16	Cylinder	82.9	76.3	0.0121	0.0131
Viking	Octagon	128	30.8	0.0078	0.0325
Explorer-11	Octagon	203	72.6	0.0049	0.0138
Explorer-17	Sphere	152	152	0.0066	0.0066
Sp. Teles.	Cylinder	192	29.5	0.0052	0.0339
OSO-7	9-sided	437	165	0.0023	0.0061
OSO-8	Cylinder	147	47.2	0.0068	0.0212
Pegasus-3	Cylinder	181	12.1	0.0055	0.0826
Landsat-1	Cylinder	123	25.2	0.0081	0.0397
ERS-1	Box	135	12.0	0.0074	0.0833
LDEF-1	12-face	169	93.1	0.0059	0.0107
HEAO-2	Hexagon	174	80.1	0.0057	0.0125
Vanguard-2	Sphere	23.5	23.5	0.0426	0.0426
SkyLab	Cylinder	410	47.1	0.0024	0.0212
Echo-1	Sphere	0.515	0.515	1.9417	1.9417

Per Table 2, $B^* = 0.01$ will be chosen as a nominal value for this research.

The location of the perigee and apogee were calculated using the state integrated over 6000 time units (TU). Visible in Figure 3, perigee and apogee exhibit the expected secular behavior. While not proof that air drag effects were correctly incorporated into the equations of motion, the plots offer a quick common-sense check because the apogee decreases and the perigee remains relatively constant over time.
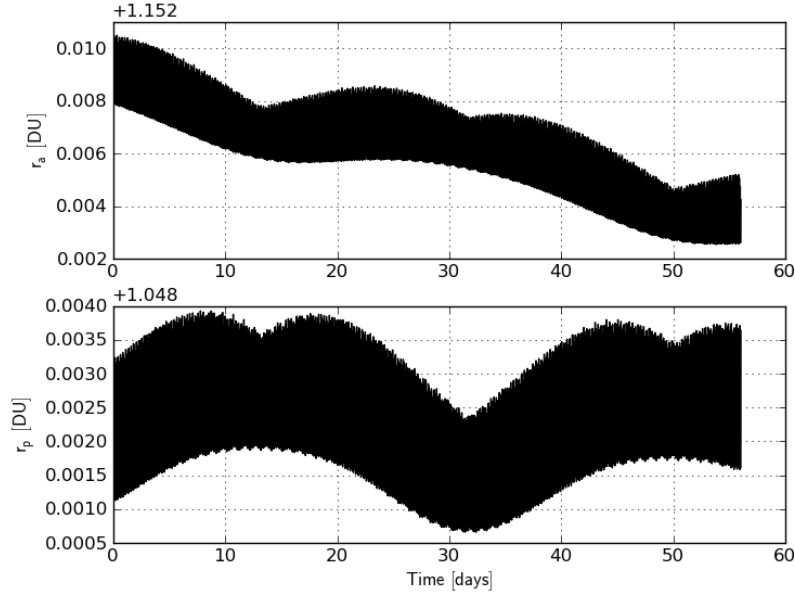

Figure 3: Apogee and Perigee Location Over Time in the Prescence of Air Drag

3.2.2.3 Third-Body Moon. The motion of the Moon is indeed complex. Accurate modeling of the Moon's orbit is complicated by third-body gravity from the Sun, as well as the Moon's inclination of 5.1° from the Earth's equator. The Moon's motion can be simplified by assuming that its orbital plane is aligned with the Earth's equator and by assuming that the Moon's orbit is circular. These assumptions are valid because the primary intent of this research is to gain understanding of how the Moon alters the motion of a satellite near the KAM Torus. In future applications with the

intent of accurately predicting satellite states, a more complex Moon model will be required.

Considering the Moon's position is required in the ECEF frame, it can be assumed that the Moon begins positioned on the ECEF x-axis at 60.27 Earth radii (60.27 distance units (DU)) and follows a circular path about the Earth, as is seen in Figure 4.
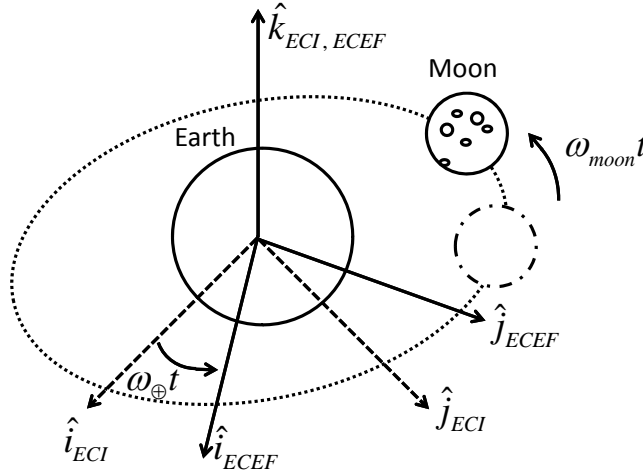

Figure 4: Earth, Moon, and ECI/ECEF Coordinate Frames

Care must be taken to correctly determine the Moon's orbital frequency with respect to the ECEF frame. Because the Earth's rotational frequency is larger than the Moon's orbital frequency, the differential between the two, $\omega_{moon} - \omega_{\oplus}$, results in the Moon rotating clockwise about the Earth in the ECEF frame:

$$
{}^{ECEF}\mathbf{r}_{moon} = r_{moon} \begin{bmatrix} \cos\left[(\omega_{moon} - \omega_{\oplus})\, t\right] \\ \sin\left[(\omega_{moon} - \omega_{\oplus})\, t\right] \\ 0 \end{bmatrix} \tag{52}
$$

where ω_{moon} is the Moon's position vector in the earth-centered-inertial (ECI) frame, $\omega_{\oplus}$ is the Earth's rotational angular velocity in the ECI frame, r_{moon} is the magnitude

of the Moon's position vector, and $^{ECEF}\mathbf{r}_{moon}$ is the Moon's position vector in the ECEF frame.

Next, the vector from the satellite to the Moon must be calculated. Referring to Figure 5, simple vector addition and subtraction yield an expression, Equation 53, for the vector between the satellite and the Moon.
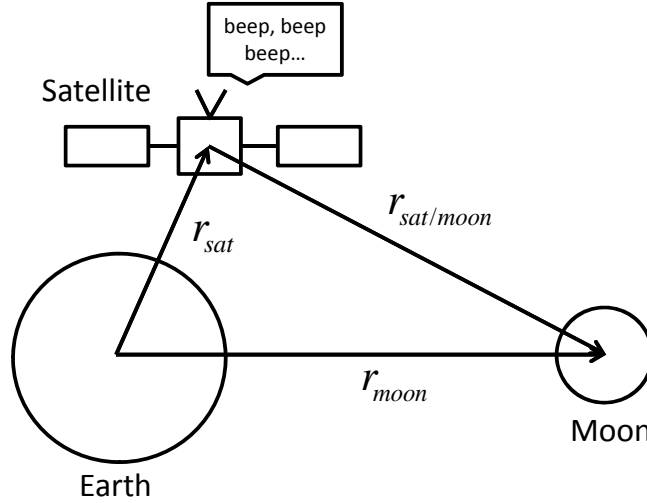

Figure 5: Determining the Position Vector from the Satellite to the Moon

$$\mathbf{r}_{sat/moon} = \mathbf{r}_{moon} - \mathbf{r}_{sat} \tag{53}$$

Referring to Equation 2 and applying $F = ma$, the acceleration of the satellite due to the Moon becomes:

$$\mathbf{a}_{sat/moon} = \frac{\mu_{moon}\mathbf{r}_{sat/moon}}{r^3_{sat/moon}} \tag{54}$$

The acceleration can then be added to the Hamiltonian partials shown in Equations 48, 49, and 50.

3.3 Torus-Perturbed Motion Comparison Loop

In the comparison loop, two initially aligned states are updated and followed in time. The reference torus state is propagated by simply updating the torus coordinates with the frequency-time relationship described by Equation 29. The perturbed state is propagated via numerical integration as described in §§3.2.1-2. Again, it is important to note that both the KAM Torus and the numerical integration include the Earth's geopotential. The only perturbations considered in this research are air drag and moon third-body effects. During each iteration of the comparison loop, the difference between the states in both physical and torus variables $\delta\mathbf{q}$, $\delta\mathbf{p}$, $\delta\mathbf{Q}$, and $\delta\mathbf{P}$, are calculated and recorded in a text file. Further discussion in this research will consider the following two definitions:

$$\delta\mathbf{X} = \begin{bmatrix} \delta\mathbf{q} \\ \delta\mathbf{p} \end{bmatrix} \tag{55}$$

$$\delta\mathbf{Y} = \begin{bmatrix} \delta\mathbf{Q} \\ \delta\mathbf{P} \end{bmatrix} \tag{56}$$

3.3.1 Collecting the Physical State Differences. Since both states have been updated after some time, Δt, the difference between the states in physical variables can be determined. Currently the torus state is known in torus variables and the perturbed state is known in physical variables. To obtain the torus state in physical variables, the same procedure utilized in §3.2.1 to extract the initial state from the torus is followed. Now with both states described in physical variables, the state differences can be calculated, expressed as shown in Equation 57:

$$\begin{bmatrix} \delta\mathbf{q} \\ \delta\mathbf{p} \end{bmatrix} = \begin{bmatrix} \mathbf{q} \\ \mathbf{p} \end{bmatrix}_{integration} - \begin{bmatrix} \mathbf{q} \\ \mathbf{p} \end{bmatrix}_{torus} \tag{57}$$

where $\mathbf{q}$ are the physical coordinates and $\mathbf{p}$ are the physical momenta.

3.3.2 Transforming Between Physical and Torus Variables. To understand the perturbation's effects on the torus coordinates and momenta, the data described in the physical variables must be transformed back to the torus variables and vice versa. This is accomplished with the Jacobian Matrix, $\frac{\partial\mathbf{Y}}{\partial\mathbf{X}}$. An estimate for this matrix can be obtained by defining three expressions of the state:

$$\mathbf{X} = \begin{bmatrix} x \\ y \\ z \\ V_x \\ V_y \\ V_z \end{bmatrix} \tag{58}$$

$$\mathbf{Y} = \begin{bmatrix} M \\ \Omega \\ \omega \\ \sqrt{\mu a} \\ \sqrt{\mu a}\sqrt{1-e^2}\cos i \\ \sqrt{\mu a}\sqrt{1-e^2} \end{bmatrix} \tag{59}$$

$$\mathbf{Z} = \begin{bmatrix} M \\ \Omega \\ \omega \\ a \\ e \\ i \end{bmatrix} \tag{60}$$

where $\mathbf{X}$ is the physical state vector, $\mathbf{Y}$ is the canonical state vector, and $\mathbf{Z}$ is the classical orbital elements state vector.

Then it follows that the Jacobian, the linear transormation between the $\mathbf{X}$ and $\mathbf{Y}$ states can be represented as Equation 61:

$$\frac{\partial \mathbf{Y}}{\partial \mathbf{X}} = \frac{\partial \mathbf{Y}}{\partial \mathbf{Z}} \frac{\partial \mathbf{Z}}{\partial \mathbf{X}} \tag{61}$$

Wiesel illustrates the development of these Jacobians in his work discussing the motion of a satellite near a torus (19). The transformations are estimates and cause some error when comparing against reality. This error proceeds from the fact that the state vectors are described with only the second zonal harmonic of the geopotential. To provide the $\mathbf{Y}$ state vector with utmost accuracy, the entire geopotential would have to be considered when developing the Jacobian which is impossible to do analytically.

The state differences in terms of the torus coordinates can be estimated as in Equation 62:

$$\begin{bmatrix} \delta \mathbf{Q} \\ \delta \mathbf{P} \end{bmatrix} = \frac{\partial \mathbf{Y}}{\partial \mathbf{X}} \begin{bmatrix} \delta \mathbf{q} \\ \delta \mathbf{p} \end{bmatrix} \tag{62}$$

The state differences, $\delta \mathbf{Q}$ and $\delta \mathbf{P}$, are now available for analysis.

3.3.2.1 Improving the Accuracy of the Jacobian. In an effort to make $\frac{\partial \mathbf{Y}}{\partial \mathbf{X}}$ more accurate, it is observed that its inverse, $\frac{\partial \mathbf{X}}{\partial \mathbf{Y}}$, can be expanded to Equation 63:

$$\frac{\partial \mathbf{X}}{\partial \mathbf{Y}} = \begin{bmatrix} \frac{\partial \mathbf{q}}{\partial \mathbf{Q}} & \frac{\partial \mathbf{q}}{\partial \mathbf{P}} \\ \frac{\partial \mathbf{p}}{\partial \mathbf{Q}} & \frac{\partial \mathbf{p}}{\partial \mathbf{P}} \end{bmatrix} \tag{63}$$

where it is seen that the left-hand side of the matrix is available from the torus via the Fourier series. At this time the author is unaware of a practical approach to obtaining exact values for the right-hand side of the matrix in Equation 63. If an approach were available, it would certainly be utilized.

The left hand portion of the matrix described in Equation 63 is presented for both cases at the initial time, $t = 0$, in Table 3.

Table 3: Comparison of Portion of Jacobian Approximated by Two-Body Problem and Exact Values from Torus #1

Two-Body Jacobian			Partial Torus Extraction Jacobian		
-6.99964e-1	-7.33130e-1	-6.67780e-1	-6.99133e-1	-7.33187e-1	-6.67433e-1
-7.85493e-1	-6.91869e-1	-8.24930e-1	-7.84273e-1	-6.91947e-1	-8.23960e-1
-3.34563e-1	-1.71706e-15	-3.12896e-1	-3.33773e-1	-4.24398e-5	-3.12385e-1
5.93428e-1	6.75994e-1	5.64685e-1	5.92915e-1	6.76079e-1	5.64441e-1
-6.28819e-1	-6.02387e-1	-6.64143e-1	-6.28013e-1	-6.02444e-1	-6.63369e-1
3.91351e-1	1.00684e-15	3.77868e-1	3.91511e-1	-1.12216e-5	3.78154e-1

A comparable presentation of data is available for the ISS Torus and is located in Appendix A, Table 11. In both cases, significant updates are made to the Jacobian in some places and in other places the two-body estimate is very close to the actual value provided by the torus. Once the update to the left-hand side of the Jacobian has been obtained, the inverse must be taken again as $\frac{\partial \mathbf{Y}}{\partial \mathbf{X}}$ is the Jacobian required for the linear transformation from physical variables to torus variables. Throughout the remainder of this work, the two versions of the Jacobian $\frac{\partial \mathbf{Y}}{\partial \mathbf{X}}$ will be referred to as the partial torus extraction (PTE) Jacobian and the two-body problem (2BP) Jacobian.

3.3.2.2 Illustration of Jacobian Accuracy Effects.   For the sake of comparing the two Jacobian versions, a relationship between the derivative of the physical state and the derivative of the torus state is derived. Starting with the linear transformation between state differences

$$\delta \mathbf{Y} = \frac{\partial \mathbf{Y}}{\partial \mathbf{X}} \delta \mathbf{X} \tag{64}$$

where $\delta \mathbf{Y}$ is the difference vector in torus variables between the perturbed, integrated state and the torus state, and $\delta \mathbf{X}$ is the difference vector in physical variables between the perturbed, integrated state and the torus state.

Next, since the state derivative relationship is desired, the time derivative is applied to Equation 64:

$$\delta \dot{\mathbf{Y}} = \frac{d}{dt} \left(\frac{\partial \mathbf{Y}}{\partial \mathbf{X}} \delta \mathbf{X} \right) \tag{65}$$

Now that the chain-rule has been applied it is apparent that the state derivative is dependent on the time derivative of the Jacobian:

$$\delta \dot{\mathbf{Y}} = \frac{d}{dt} \left(\frac{\partial \mathbf{Y}}{\partial \mathbf{X}} \right) \delta \mathbf{X} + \frac{\partial \mathbf{Y}}{\partial \mathbf{X}} \delta \dot{\mathbf{X}} \tag{66}$$

Selectively expanding the differences yields

$$\dot{\mathbf{Y}}_{int} - \dot{\mathbf{Y}}_{torus} = \frac{d}{dt} \left(\frac{\partial \mathbf{Y}}{\partial \mathbf{X}} \right) \delta \mathbf{X} + \frac{\partial \mathbf{Y}}{\partial \mathbf{X}} \left(\dot{\mathbf{X}}_{int} - \dot{\mathbf{X}}_{torus} \right) \tag{67}$$

where $\dot{\mathbf{Y}}_{int}$ is the perturbed, integrated state derivative transformed into torus state variables, $\dot{\mathbf{X}}_{int}$ is the perturbed, integrated state derivative in physical state variables,

$\dot{\mathbf{Y}}_{torus}$ is the reference torus state derivative transformed into torus state variables, and $\dot{\mathbf{X}}_{torus}$ is the reference torus state derivative in physical state variables.

Through selective application of the definition of the time derivative:

$$\dot{\mathbf{Y}}_{int} - \frac{\partial}{\partial t}\mathbf{Y}_{torus} = \frac{d}{dt}\left(\frac{\partial \mathbf{Y}}{\partial \mathbf{X}}\right)\delta\mathbf{X} + \frac{\partial \mathbf{Y}}{\partial \mathbf{X}}\left(\dot{\mathbf{X}}_{int} - \frac{\partial}{\partial t}\mathbf{X}_{torus}\right) \quad (68)$$

Next, rearranging

$$\dot{\mathbf{Y}}_{int} = \frac{d}{dt}\left(\frac{\partial \mathbf{Y}}{\partial \mathbf{X}}\right)\delta\mathbf{X} + \frac{\partial \mathbf{Y}}{\partial \mathbf{X}}\dot{\mathbf{X}}_{int} - \frac{\partial \mathbf{Y}}{\partial \mathbf{X}}\frac{\partial}{\partial t}\mathbf{X}_{torus} + \frac{\partial}{\partial t}\mathbf{Y}_{torus} \quad (69)$$

With the cancellation of terms, the expression becomes

$$\dot{\mathbf{Y}}_{int} = \frac{d}{dt}\left(\frac{\partial \mathbf{Y}}{\partial \mathbf{X}}\right)\delta\mathbf{X} + \frac{\partial \mathbf{Y}}{\partial \mathbf{X}}\dot{\mathbf{X}}_{int} \quad (70)$$

Equation 70 has an important ramification. When perturbed motion is integrated and compared against the reference torus state some state difference $\delta\mathbf{X}$ will necessarily exist. The state difference doesn't make Equation 70 unusable, but some complexity is incurred in the requirement to calculate the time derivative of the Jacobian. With the additional choice of evaluating the Jacobian with the unperturbed, integrated motion the additional simplification, $\delta\mathbf{X} = \mathbf{0}$, can be made. This simplification yields Equation 71:

$$\dot{\mathbf{Y}}_{int} = \frac{\partial \mathbf{Y}}{\partial \mathbf{X}}\dot{\mathbf{X}}_{int} \quad (71)$$

where $\dot{\mathbf{X}}$ is available as Equations 45, 46, 47, 48, 49, and 50. Again, Equation 71 is only valid when the integration and torus states (coordinates and momenta) are aligned near-perfectly, otherwise Equation 70 must be used.

The time derivatives of the torus coordinates of the unperturbed motion near the reference torus were calculated utilizing the two-body problem Jacobian as well as the Jacobian updated via the torus extraction. It is expected that the coordinate derivatives should closely approximate the torus basis frequencies. The results shown in Figure 6 illustrate that the PTE Jacobian yields more reasonable results for instantaneous $\dot{Q}_1$ values than the two-body Jacobian. The PTE Jacobian result exhibits small oscillations about the basis frequency, ω_1, while the 2BP Jacobian result oscillates to a greater degree.
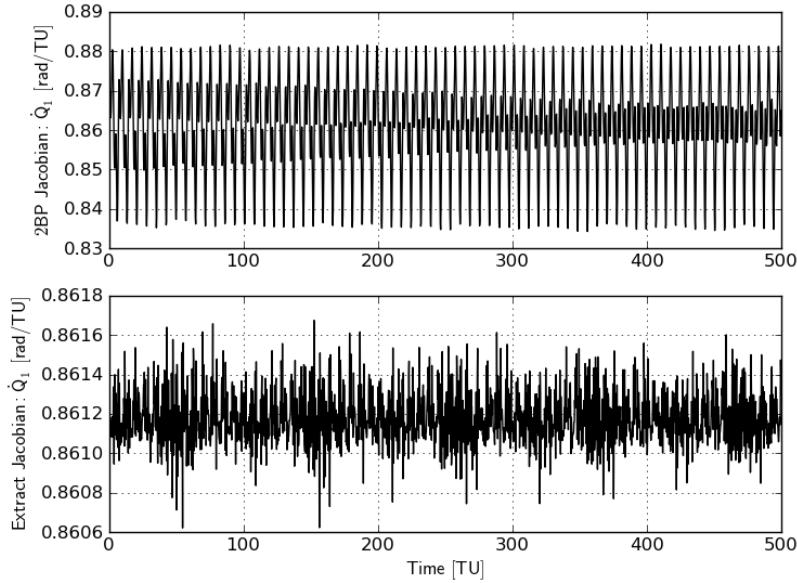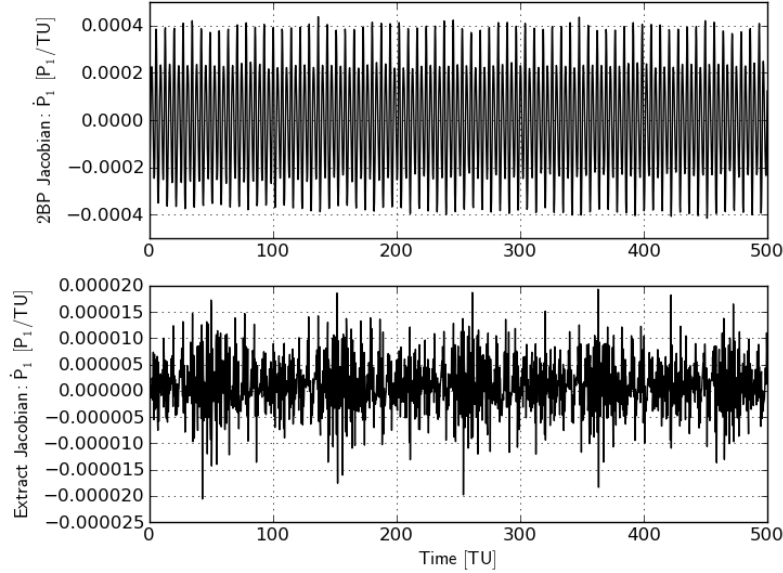

Figure 6: Time Derivative of Unperturbed Torus Coordinate Q_1 Utilizing the Two-Body Jacobian and the Partial Torus Extraction Jacobian

Even more importantly, the averaged value of $\dot{Q}_1$ from the PTE Jacobian is closer to the basis frequency than the averaged value of $\dot{Q}_1$ from the 2BP Jacobian. The results for all three coordinate rates are summarized in Table 4.

Table 4: Averages of Coordinate Time Derivatives Calculated Using the Two-Body Jacobian & the Partial Torus Extraction Jacobian

	$\dot{Q}_1$ [rad/TU]	$\dot{Q}_2$ [rad/TU]	$\dot{Q}_3$ [rad/TU]
Torus Frequency	0.86115953	-0.05983301	0.00158568
2BP Jacobian	0.86123874	-0.05983382	0.00150735
PTE Jacobian	0.86117945	-0.05983281	0.00156017

In addition, for the unperturbed (no perturbing forces other than the geopotential) motion near the reference torus, it is expected that $\dot{\mathbf{P}} = \mathbf{0}$. The plots in Figure 7 demonstrate that while both the 2BP and PTE Jacobian results oscillate about zero for $\dot{P}_1$, the magnitude of the oscillations produced using the PTE Jacobian are much closer to zero.

Figure 7: Time Derivative of Unperturbed Torus Momentum P1 Utilizing the Two-Body Jacobian and the Partial Torus Extraction Jacobian

Comparable results are seen in plots for $\dot{Q}_2$, $\dot{Q}_3$, $\dot{P}_2$, and $\dot{P}_3$ which are included in Appendix A, Figure 41, Figure 42, Figure 43, and Figure 44. The average time derivatives for the momenta using both Jacobians are summarized in Table 5.

Table 5: Averages of Momenta Derivatives Calculated Using the Two-Body Jacobian
& the Partial Torus Extraction Jacobian

	$\dot{\mathbf{P}}_1$ [rad/TU]	$\dot{\mathbf{P}}_2$ [rad/TU]	$\dot{\mathbf{P}}_3$ [rad/TU]
Ideal Torus Value	0	0	0
2BP Jacobian	9.3×10^{-7}	8.4×10^{-7}	9.4×10^{-7}
PTE Jacobian	1.0×10^{-6}	8.7×10^{-7}	1.0×10^{-6}

While the values for time derivatives of the momenta are all practically zero, the 2BP Jacobian case appears slightly more accurate than the PTE Jacobian case. All factors considered, the PTE Jacobian is clearly preferred for two reasons. First, the coordinate time derivatives more closely approximate the torus basis frequencies. Second, at any given time the values of the coordinates derivatives and momenta derivatives remain closer to the theoretical torus values described by the basis frequencies. As mentioned earlier, while the Jacobians $\frac{\partial \mathbf{Y}}{\partial \mathbf{X}}$ and $\frac{\partial \mathbf{X}}{\partial \mathbf{Y}}$ were improved by updating the left-hand side of $\frac{\partial \mathbf{X}}{\partial \mathbf{Y}}$, important accuracy improvements may be gained if a method for obtaining exact values for the right-hand side is developed.

The effects of the improvement of the Jacobian are even more dramatically seen when applied to Torus #2, the ISS Torus, as shown in Figure 8.

The coordinate rate $\dot{Q}_1$ which is the frequency of mean anomaly, wildly oscillates between 0 $[rad/TU]$ and 2.5 $[rad/TU]$ in the two-body problem Jacobian estimate case. The actual frequency, 0.92 $[rad/TU]$ is much more closely approximated via the PTE Jacobian. Note that a zero value for the rate of change of mean anomaly infers that the satellite is essentially stopped in it's orbit for a short period of time which is not realistic and tells us that the two-body estimate is not accurate in comparison to the PTE Jacobian. Similar results are seen in plots for $\dot{Q}_2$, $\dot{Q}_3$, $\dot{P}_2$, $\dot{P}_2$, and $\dot{P}_3$ which are included in Appendix A, Figures 45, 46, 47, 48, and 49.
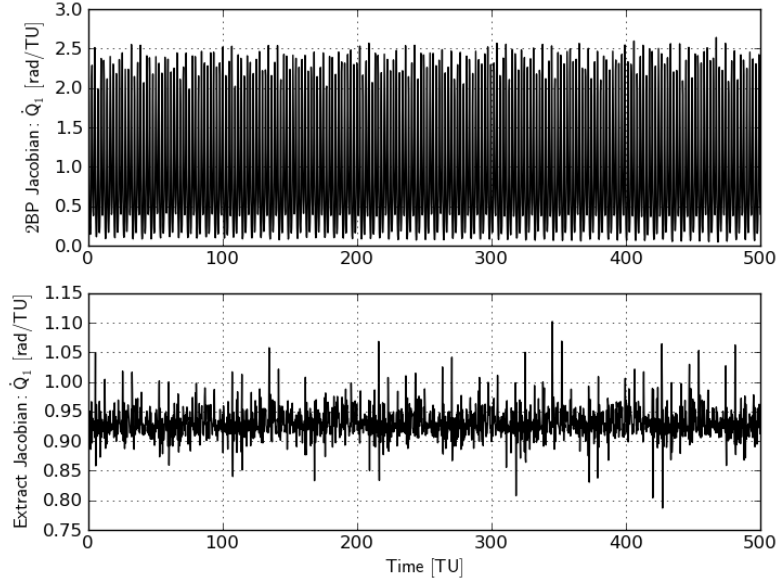
Figure 8: Time Derivative of Unperturbed Torus #2 (ISS) Coordinate Q_1 Utilizing the Two-Body Jacobian and the Partial Torus Extraction Jacobian

3.3.3   Update of the Torus Phase.   Nominally, the coordinates of the KAM Torus update linearly with time, but it must be considered that motion near the torus is being evaluated. When describing perturbed motion near the torus, the coordinates no longer increase in an exclusively linear manner.

Over time the perturbed motion will exhibit a non-negligible phase difference in each of the coordinates. The growth of the magnitude of position error over time for unperturbed motion, drag perturbed motion, and third-body lunar perturbed motion near the reference torus is shown in Figure 9.

38
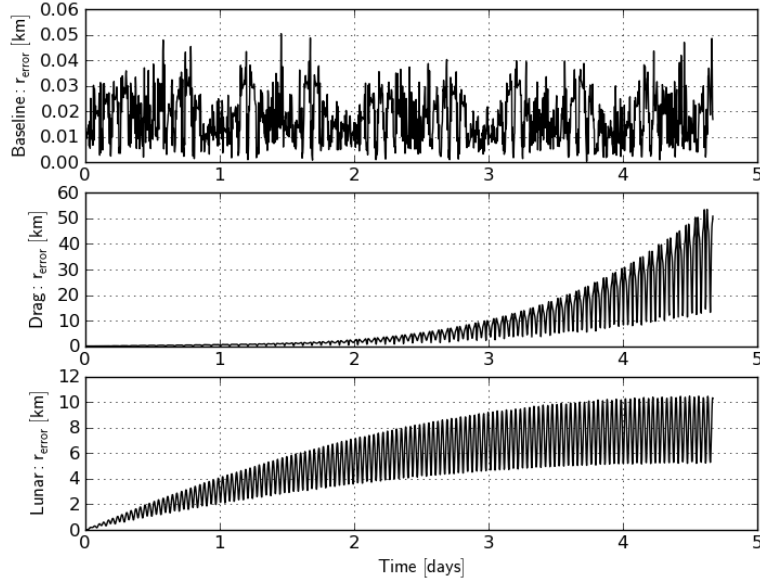
Figure 9: Actual Error for Three Cases of Motion Near a Reference Torus

The error seen in Figure 9 is not solely due to phase offset but also includes error due to momenta differences between the reference torus and the perturbed motion. The baseline case shows little error accumulation but both perturbed cases produce substantial error over several days. The error magnitude was calculated per Equation 72 and Equation 73:

$$\delta \mathbf{q} = \mathbf{q}_{int} - \mathbf{q}_{torus} \tag{72}$$

$$r_{error} = \sqrt{\delta x^2 + \delta y^2 + \delta z^2} \tag{73}$$

where $\delta \mathbf{q}$ is the difference vector of the physical coodinates between the perturbed, integrated state and the reference torus state, $\mathbf{q}_{int}$ is the physical coordinate vector of the perturbed, integrated state, $\mathbf{q}_{torus}$ is the physical coordinate vector of the reference torus state, r_{error} is the magnitude of the position error between the two states, and δx,

39

δy, and δz are differences in physical coordinates between the perturbed, integrated state and the reference torus state.

Phase differences have an additional consequence beyond that described above. As the perturbed state diverges from the reference torus state, errors will be magnified because the Jacobian method used to transform between physical and torus coordinates is a linear transformation. Over time, the magnitude of $\delta\mathbf{Q}$ at each time step will grow large enough that the linear transformation using the Jacobian, $\frac{\partial\mathbf{X}}{\partial\mathbf{Y}}$, will no longer be valid.

If the phase discrepancy is ignored and the linear assumption is violated the numerical results become invalid. The total position error magnitude over time calculated per Equations 73 and 74.

$$\delta\mathbf{X} = \frac{\partial\mathbf{X}}{\partial\mathbf{Y}} \begin{bmatrix} \delta\mathbf{Q} \\ \delta\mathbf{P} \end{bmatrix} \tag{74}$$

The total position error magnitude over time is shown in Figure 10.
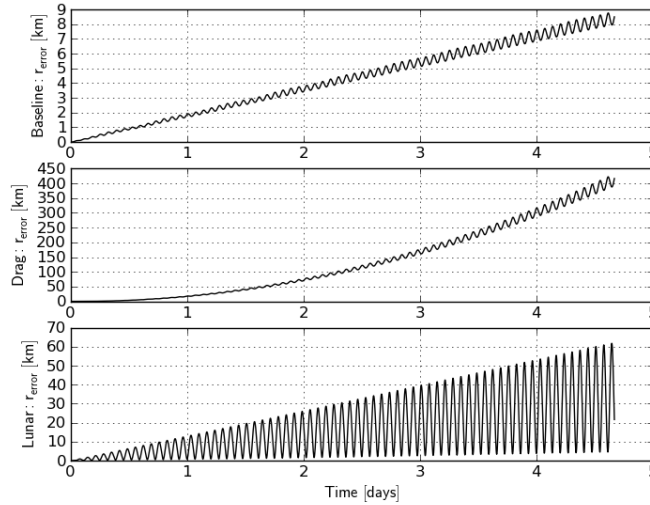
Figure 10: Error Magnitude Calculated with Linear Assumption Violated

The linear transformation barely holds for the baseline case which means that even a very small amount of discrepancy between the motion near the torus and the reference torus causes the linearization to magnify the error due to differences in the coordinates. The errors in the perturbed cases grow unreasonable levels in just days which is not expected for air drag or lunar third-body effects (compare with accurate error plots in Figure 9). Per this observation, the torus coordinates absolutely must be updated at each time step if knowledge is to be gained from analyzing differences in the torus coordinates and momenta. The torus coordinates will be updated as follows

$$\mathbf{Q}_{torus}(t) = \mathbf{Q}_{torus0} + \boldsymbol{\omega}t + \boldsymbol{\Phi}(t) \tag{75}$$

where $\mathbf{Q}_{torus}$ is the coordinate vector at a given time t, $\mathbf{Q}_{torus0}$ is the initial coordinate vector at initial time t_0, $\boldsymbol{\omega}$ is the torus basis frequency vector, and $\boldsymbol{\Phi}$ is the phase vector at a given time t.

The phase vector is accumulated over time in order to compare the perturbed motion with the closest location on the reference torus at any time such that:

$$\boldsymbol{\Phi} = \mathbf{Q}_{int} - \mathbf{Q}_{torus} \tag{76}$$

An important distinction must be made now that the reference torus coordinates are updated to minimize error with the perturbed motion at every time step. At each time step, additional phase, designated as $\delta\boldsymbol{\Phi}$, will be added to the current phase to keep the two states, perturbed and reference torus, aligned.

Said another way, $\delta\boldsymbol{\Phi}$ is the unique amount of phase added to the total phase at each time step such that

$$\delta\mathbf{\Phi} = \mathbf{Q}_{int} - \mathbf{Q}_{torus} - \mathbf{\Phi} \qquad (77)$$

Note that while phase accumulation, $\mathbf{\Phi}$, helps to minimize the error at any time step, it does not remove all error as $\delta\mathbf{P}$ has not been accounted for. A difference in torus momenta, $\delta\mathbf{P}$, implies that the motion has moved from the torus to an adjacent torus. In this case, since the motion near the reference torus is under consideration, adjacent tori are not considered, but rather $\delta\mathbf{P}$ will be evaluated as it pertains to inducing state error.

IV. Results

4.1 Understanding Differentials in the Torus Coordinates and Momenta

A torus has coordinates that increment linearly with time and momenta that remain constant with time. When motion near a torus is perturbed by drag or third-body lunar effects, non-linear changes are seen in the coordinates as additional phase not present in the reference torus.

Per Equation 77, at each time step phase differences for each coordinate will be collected as

$$\delta\boldsymbol{\Phi} = \begin{bmatrix} \delta\Phi_{Q1} \\ \delta\Phi_{Q2} \\ \delta\Phi_{Q3} \end{bmatrix} \tag{78}$$

Clearly visible in Figure 11, the Q_1 coordinate grows faster over time in the drag case and in the lunar case exhibits some type of non-linear behavior.
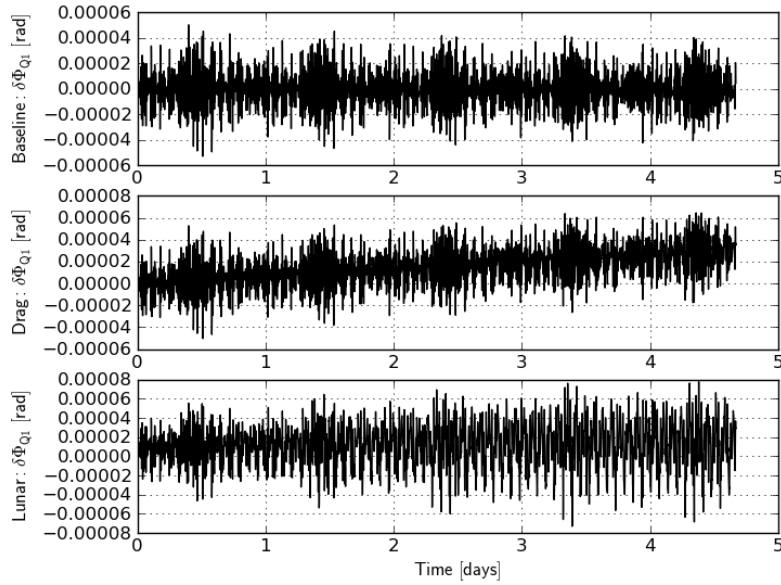
Figure 11: Coordinate Q1 Phase Differences for Baseline, Drag, and Lunar Cases

While Figure 11 makes it fairly obvious that the drag and lunar cases show non-linear changes in the coordinates, the plot does not make clear how the coordinate changes in the long run. This is remedied by observing the phase accumulation – the amount of phase required to most closely align the state of the reference torus with that of the state of the perturbed motion. The phase accumulation for Q_1 is shown in Figure 12.
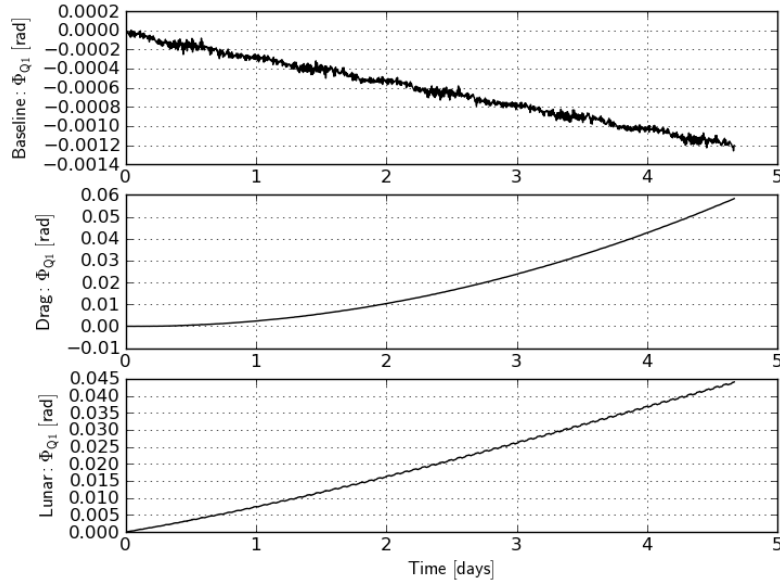
Figure 12: Coordinate Q1 Phase Accumulation for Baseline, Drag, and Lunar Cases

In theory, the phase accumulation for the baseline case should be zero for all time, but the plot has a small level of drift error. The source of this error is most likely that the torus was not an exact fit to the integrated unperturbed data. For the drag case, the phase accumulation has a quadratic nature which is likely associated with the exponential density characteristics of the Earth's atmosphere. Since Q_1 is approximately the mean anomaly of an orbit, it is reasonable that as an orbiting satellite loses energy due to drag, its semi-major axis is decreased and its velocity will

increase, thus increasing $\dot{M}$. Again, the lunar case exhibits a deviation from linear behavior but it is difficult to characterize at this time scale.

Referring back to §2.1.2.1 on drag effects, Equation 20, it is predicted that drag will not affect the RAAN. Q_2 is approximately equivalent to RAAN, and in Figure 13 it is seen that additional phase is accumulated due to drag but the magnitude of Φ_{Q2} is very small compared to Q_2.
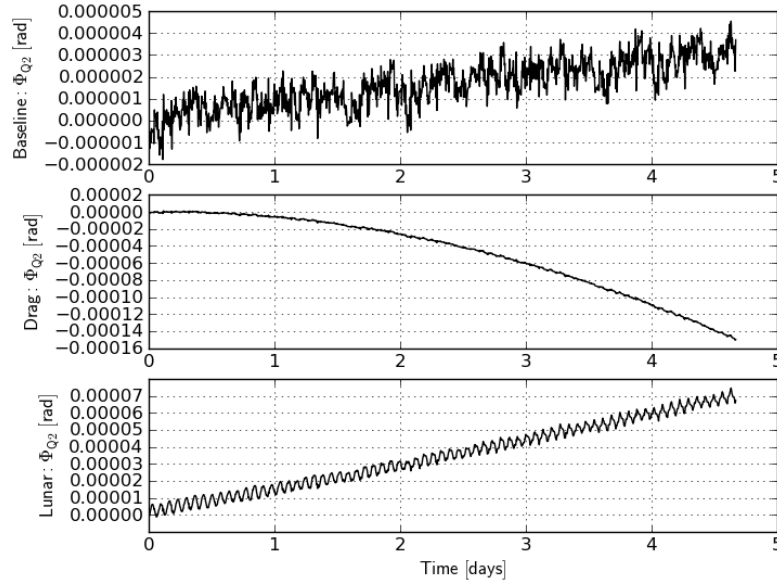
Figure 13: Coordinate Q2 Phase Accumulation for Baseline, Drag, and Lunar Cases

Q_3 which is synonymous with AP exhibits quadratic behavior and again the lunar case has definite effects as well, as shown in Figure 14.

Thus far, torus coordinates have been discussed, but the momenta must be considered as well. The non-perturbed torus should have constant momenta. Non-constant momenta imply that the satellite has moved from the reference torus to an adjacent torus. An adjacent torus is characterized as similar to the reference torus but with slightly different frequencies – which means that the torus coordinates will increment linearly at different basis frequencies.
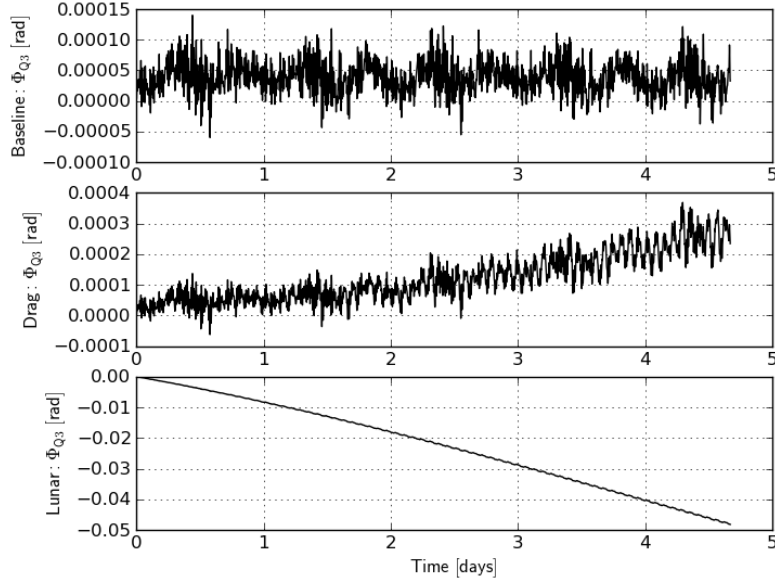
Figure 14: Coordinate Q3 Phase Accumulation for Baseline, Drag, and Lunar Cases

Figure 15 shows that as expected, the P_1 momentum is fairly constant for the baseline case, while the drag and lunar cases exhibit a linear rate of change. The change in momenta, δP_2 and δP_3, behave similarly and are shown as Figure 52 and Figure 53 in Appendix A.

Assuming the reference torus is used to predict the location of a perturbed satellite at a given time, some state error exists due to the coordinate and momenta offsets from the reference torus, $\delta\boldsymbol{\Phi}$ and $\delta\mathbf{P}$ respectively. As detailed in §3.3.1 / Equation 57, $\delta\mathbf{q}$ and $\delta\mathbf{p}$ are available, so the magnitude of the error can be calculated as per Equation 79 and Equation 80:

$$r_{error} = \sqrt{\delta x^2 + \delta y^2 + \delta z^2} \tag{79}$$

$$V_{error} = \sqrt{\delta V x^2 + \delta V y^2 + \delta V z^2} \tag{80}$$

where r_{error} and V_{error} are the position and velocity error magnitudes, respectively.

46
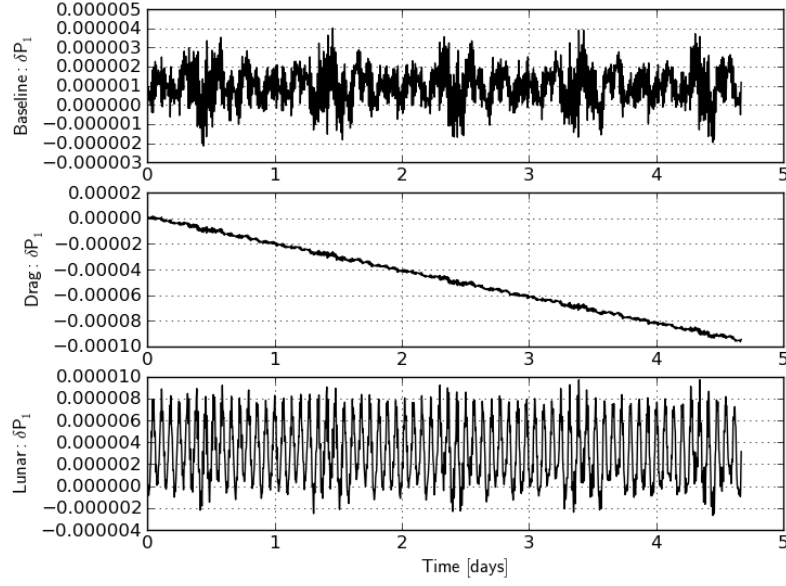
Figure 15: Momentum Differences, δP_1, for Baseline, Drag, and Lunar Cases

The total position and velocity error for the three cases are shown in Figure 16 and Figure 17, respectively.
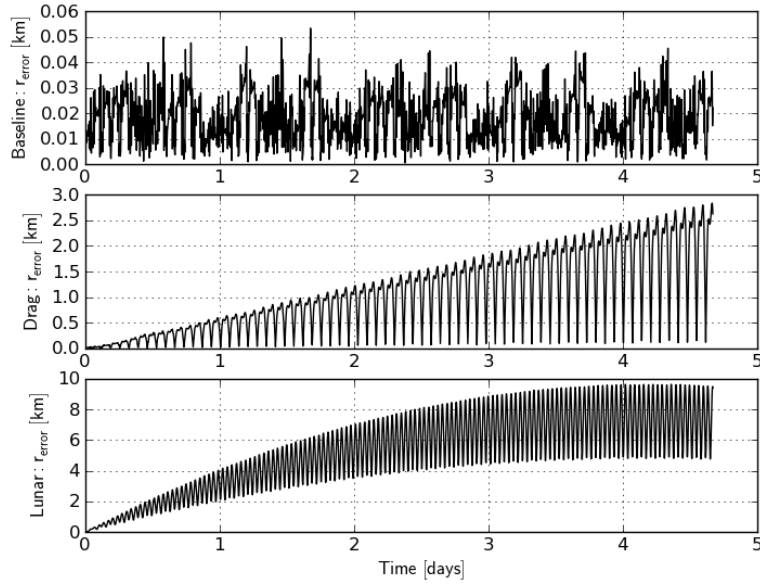
Figure 16: Total Position Error for Baseline, Drag, and Lunar Cases
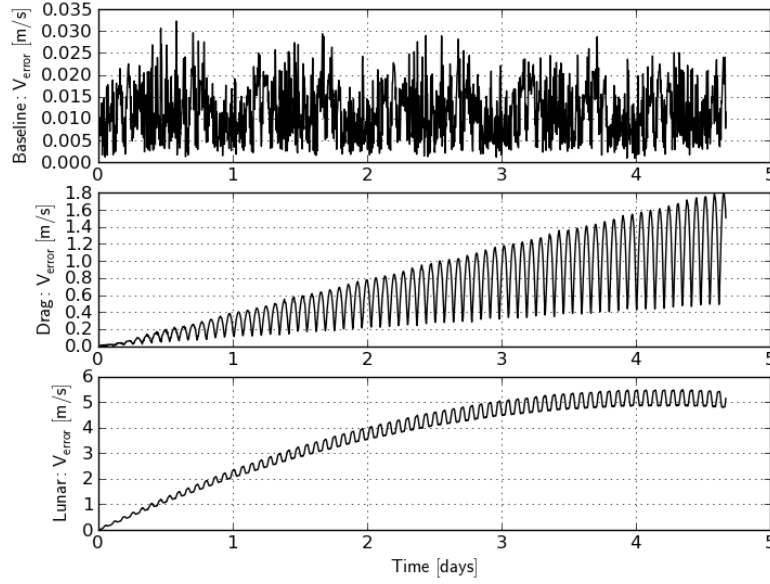
Figure 17: Total Velocity Error for Baseline, Drag, and Lunar Cases

The oscillations seen in the drag case in Figure 16 approach zero kilometers error in every cycle. This phenomenon is associated with the satellite being located at the perigee. The errors for the drag and lunar cases seem large, but it is important to note that 3-10 km of error when the position vector magnitude is on the order of 7000 km is just over 1% error. It is tempting to believe that this error can be reduced by accurately predicting the effects of drag and lunar third-body on the torus. The approach followed thus far has already updated the torus coordinates after each time step. Therefore, the remaining error is present in the momenta and cannot be removed with a state update without jumping to an adjacent torus. Rather, this approach has demonstrated that updating the torus coordinates is not just beneficial but absolutely necessary in applications that require use of the Jacobian, and that the remaining error resides in the momenta differences.

4.2 Isolating Primarily Effected Torus Variables

To understand which, if any, of the specific coordinates/momenta are most affected by the perturbations, assume a change in only one coordinate or momentum and calculate the associated error. For example:

$$\delta \mathbf{X} = \frac{\partial \mathbf{X}}{\partial \mathbf{Y}} \begin{bmatrix} 0 \\ \delta \Phi_{Q2} \\ 0 \\ 0 \\ 0 \\ 0 \end{bmatrix} \tag{81}$$

Note that it has already been shown that differences in the coordinates cause large errors and therefore the torus coordinates are updated with phase; therefore, it is expected that the coordinates should not contribute much error since at any given time step the only error in the coordinates is $\delta \mathbf{\Phi}$ as $\mathbf{\Phi}$ is already accounted for. The total error per associated coordinate or momentum is calculated using Equations 79 and 80 . Figures 18, 19, 20, 21, 22, and 23 show the total position error over time due to $\delta \Phi_{Q1}$, $\delta \Phi_{Q2}$, $\delta \Phi_{Q3}$, δP_1, δP_2, and δP_3, respectively.
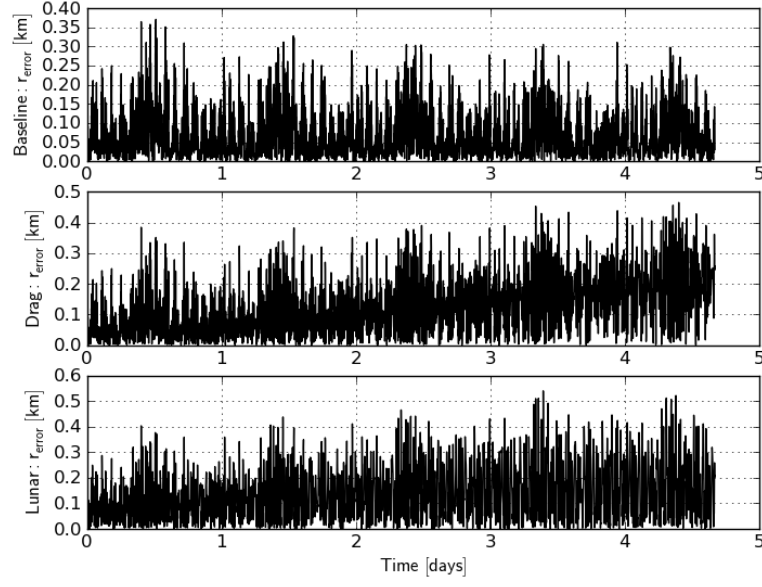
Figure 18: Total Position Error Due to $\delta\Phi_{Q1}$ for Baseline, Drag, and Lunar Cases
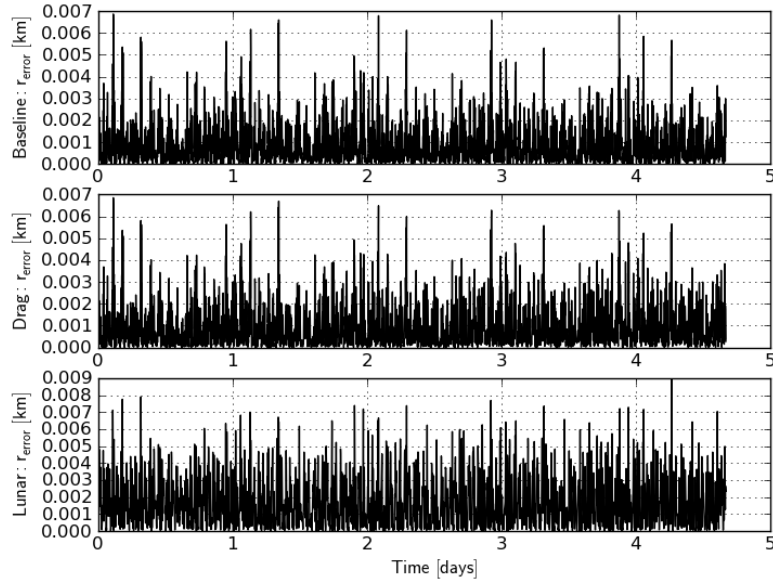
Figure 19: Total Position Error Due to $\delta\Phi_{Q2}$ for Baseline, Drag, and Lunar Cases
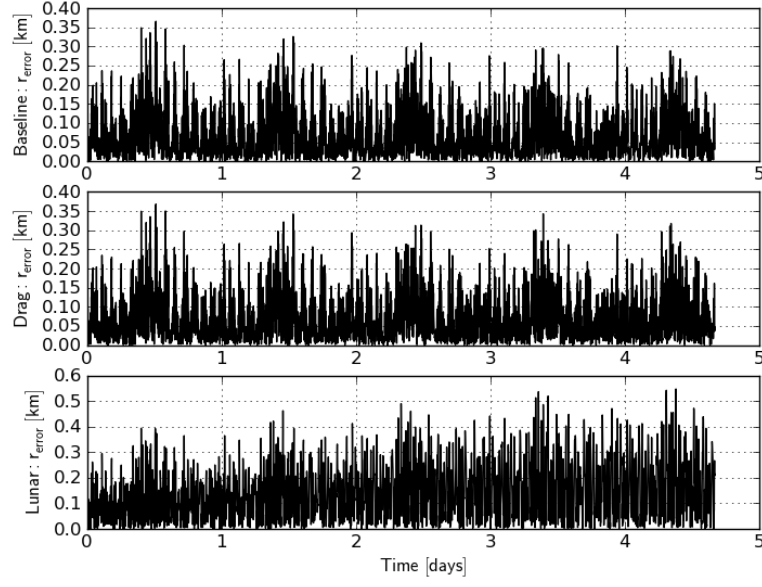
Figure 20: Total Position Error Due to $\delta\Phi_{Q3}$ for Baseline, Drag, and Lunar Cases
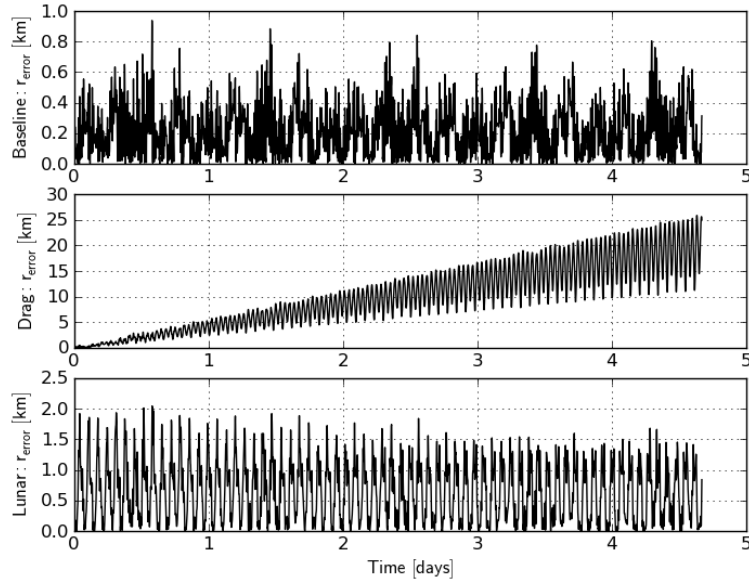
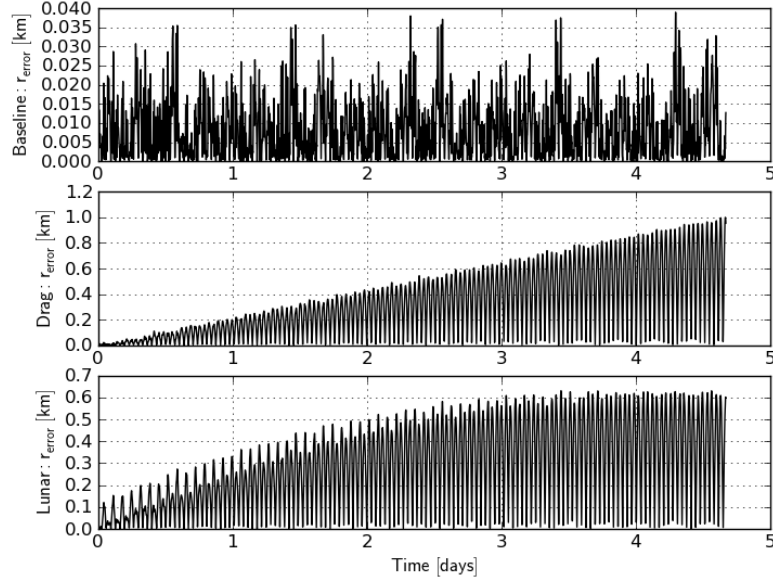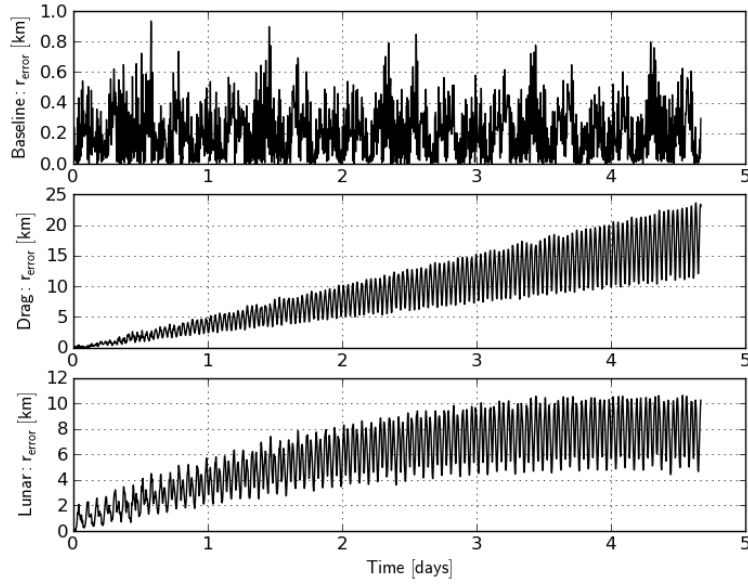Figure 21: Total Position Error Due to δP_1 for Baseline, Drag, and Lunar Cases

Figure 22: Total Position Error Due to δP_2 for Baseline, Drag, and Lunar Cases

Figure 23: Total Position Error Due to δP_3 for Baseline, Drag, and Lunar Cases

As expected, the error resulting from each coordinate is minimal, mainly due to the approach of updating the coordinate phase after each time step. The error contributed from δP_1 and δP_2 is on the same order as the coordinates, but the error due to δP_3 is significant. This indirectly confirms the observation that updating the coordinates is necessary and error resides in the momenta offsets.

4.3 Methods to Characterize Air Drag Effects on KAM Torus Coordinates and Momenta

It is not sufficient to be able to numerically integrate a specific case or even to view data collected in the past to see how a satellite has traversed or deviated from a reference torus. The capability sought is to be able to predict the effects of air drag and third-body lunar effects on motion near a given torus.

With that thought in mind, it is intuitive to attempt to establish a method of coordinate rate estimating by manipulating the results discussed in §4.1. Two approaches, based on the same data set, will be considered. First, the coordinate differences may be divided by the time-step and then fit via linear least squares resulting in coordinate time derivatives that are functions of time. Second, the phase accumulation for each coordinate can be divided by the associated time vector then fit via linear least squares to provide a function returning the phase estimate for each coordinate at a given time.

4.3.1 Estimated Differences of Coordinate Time Derivatives. Time derivatives of the coordinates are useful for applications that require numerical integration and also for comparison against the basis frequencies of the reference torus. In the comparison loop described in §3.3, the phases of the coordinates are updated at every time step. This update results in a collection not of the difference between unper-

turbed and perturbed coordinates, but rather a phase difference, $\delta\mathbf{\Phi}$, between the current and previous time step that does not include the summed phase from all previous time steps. The differences between the reference torus coordinate derivatives and the perturbed motion coordinate derivatives are calculated as

$$\delta\dot{\mathbf{Q}} = \frac{\delta\mathbf{\Phi}}{\Delta t} \tag{82}$$

The results of approximating the coordinate time derivative differences for two different time periods, 500 TU and 6000 TU (about 5.5 days and 56 days), are summarized in Table 6.

Table 6: Intercept and Slope for Torus #1 Coordinates Rates Via Linear Least Squares

Coordinate Rate	500 TU @ $\Delta t = 0.25$ TU		6000 TU @ $\Delta t = 0.25$ TU	
	Intercept [rad/TU]	Slope [rad/TU^2]	Intercept [rad/TU]	Slope [rad/TU^2]
$\delta\dot{Q}_1$	-3.006×10^{-6}	4.782×10^{-7}	-2.440×10^{-5}	4.800×10^{-7}
$\delta\dot{Q}_2$	1.322×10^{-8}	-1.250×10^{-9}	6.831×10^{-8}	-1.244×10^{-9}
$\delta\dot{Q}_3$	5.153×10^{-7}	-1.884×10^{-10}	-1.182×10^{-7}	1.995×10^{-9}

Comparing the results for the linear least squares fits for the time periods of 500 TU and 6000 TU, it is seen that the different time spans don't make a significant difference especially with respect to the function slopes of $\delta\dot{Q}_1$ and $\delta\dot{Q}_2$. The intercept values seem to vary but they are on the order of the slopes and are therefore insignificant after even a few time-steps. The time derivative of coordinate δQ_3 exhibits behavior different from the other two – unexpectedly, the slope for the 500 TU integration is negative while the slope for the 6000 TU integration is positive. The raw data with the linear fits superimposed for all three coordinates for both 500 TU/4.5 days and 6000 TU/56 days are shown in Figure 24 and Figure 25.

Of particular interest is the long period oscillation in $\dot{Q}_3$ beginning to be visible in the 56 day plot. The non-symmetrical nature of oscillation certainly explains why
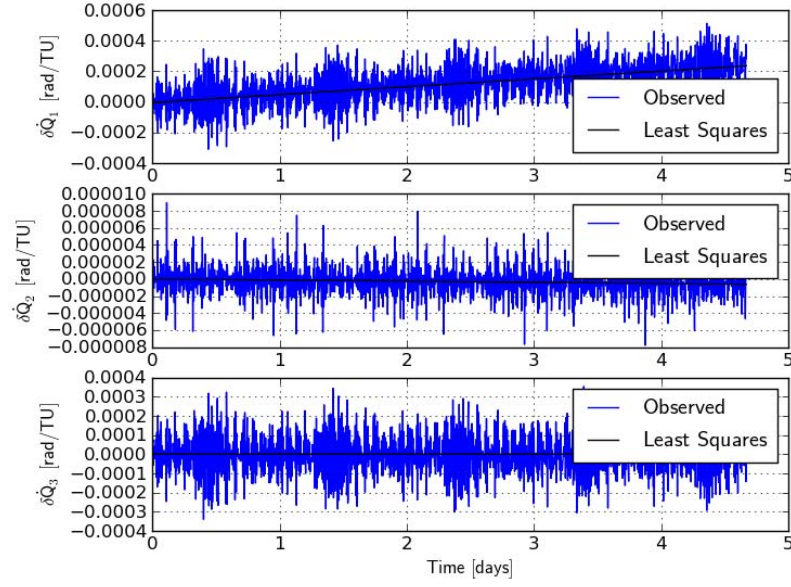
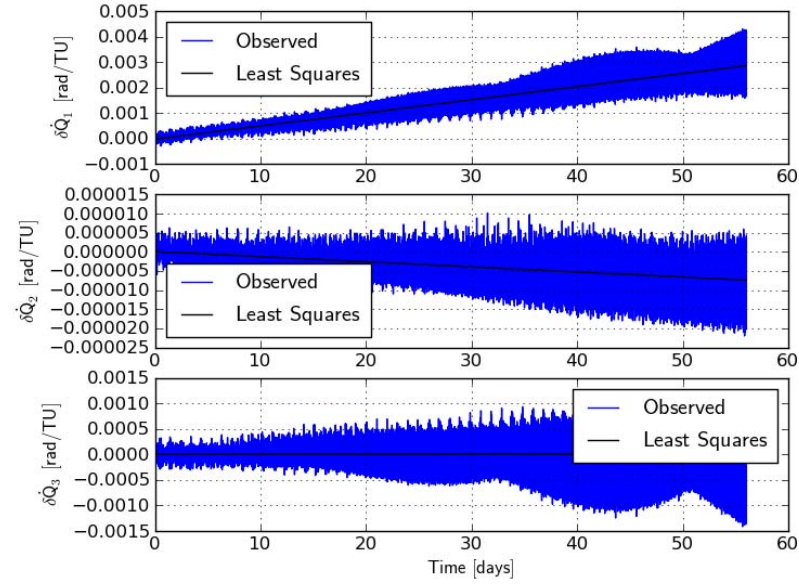Figure 24: Coordinate Time Derivative Differences and Linear Fits for 4.5 Days

Figure 25: Coordinate Time Derivative Differences and Linear Fits for 56 Days

the linear slope of the least-squares fit is changing from negative to positive in the 4.5 day and 56 day cases, respectively.

With the linear least squares fit results, the torus coordinate rates can now be described as

$$\dot{\mathbf{Q}}(t) = \boldsymbol{\omega} + \delta\dot{\mathbf{Q}}_{intercept}t + \delta\dot{\mathbf{Q}}_{slope}t^2 \tag{83}$$

where $\delta\dot{\mathbf{Q}}_{intercept}$ is the linear least squares intercept for $\delta\dot{\mathbf{Q}}$ and $\delta\dot{\mathbf{Q}}_{slope}$ is the linear least squares slope for $\delta\dot{\mathbf{Q}}$.

Equation 83 can now be used for applications in which numerical integration of the torus coordinates is required.

4.3.2 Coordinate Phases at a Given Time. During the comparison loop described in §3.3 the phase history previously termed phase accumulation, was collected over time. This phase history appears to have a quadratic nature when plotted. When the phase time history is divided by the time vector, the resulting data is linear and appropriate for linear least squares. The slope and intercept values from the linear least squares fit are summarized in Table 7 and the approximate functions are compared against the raw data in Figure 26 and Figure 27.

Table 7: Intercept and Slope for Torus #1 Coordinates Phase Per Time Via Linear Least Squares

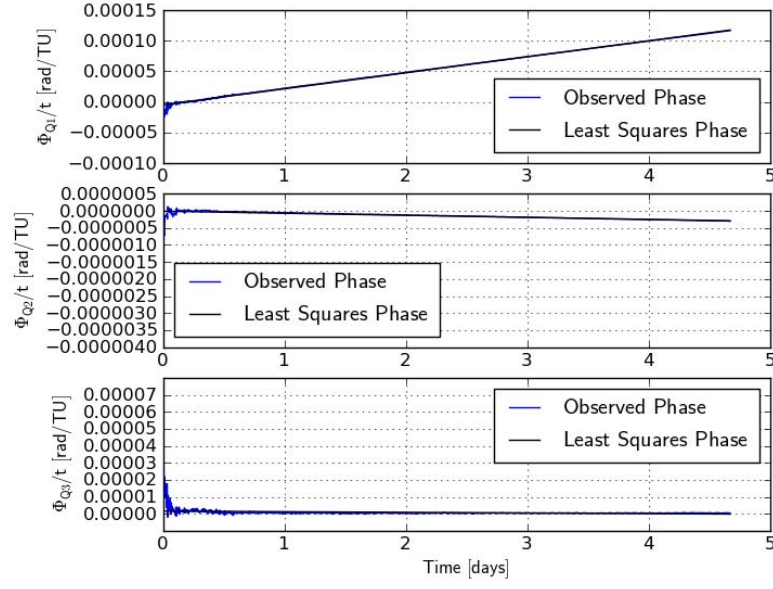| Coordinate Phase	500 TU @ $\Delta t = 0.25$ TU		6000 TU @ $\Delta t = 0.25$ TU	
	Intercept [rad/TU]	Slope [rad/TU^2]	Intercept [rad/TU]	Slope [rad/TU^2]
Φ_{Q1}/t	-4.626×10^{-6}	2.441×10^{-7}	-7.646×10^{-6}	2.358×10^{-7}
Φ_{Q2}/t	-6.977×10^{-9}	-5.649×10^{-10}	1.976×10^{-8}	-6.098×10^{-10}
Φ_{Q3}/t	1.644×10^{-6}	-3.478×10^{-9}	2.142×10^{-7}	9.147×10^{-10}

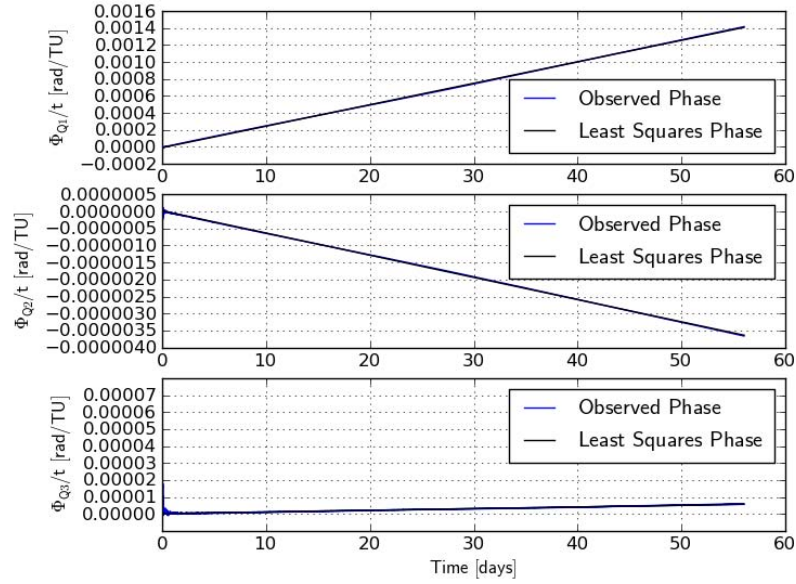Figure 26: Coordinate Phase Per Time and Linear Fits for 4.5 Days

Figure 27: Coordinate Phase Per Time and Linear Fits for 56 Days

The intercept and slope information can be used to incorporate air drag effects directly into KAM Torus applications for this specific satellite, orbit, and time, without the need for numerical integration per Equation 84:

$$\mathbf{Q}(t) = \boldsymbol{\omega}t + (\boldsymbol{\Phi}_{intercept} + \boldsymbol{\Phi}_{slope}t)\, t \tag{84}$$

where $\boldsymbol{\Phi}_{intercept}$ is the linear least squares intercept for $\boldsymbol{\Phi}$ and $\boldsymbol{\Phi}_{slope}$ is the linear least squares slope for $\boldsymbol{\Phi}$.

Various trade studies and analyses would have to be performed to determine how long the combined KAM Torus – Air Drag Characterization would provide valid solutions. As discussed earlier, this coordinate update does not account for differences in momenta which do contribute considerably to error in state knowledge.

4.3.3 Momenta Differences. The momenta data collected from the comparison loop differs from the coordinate data in that it is not utilized at any time to update the reference torus state. Because the momenta difference data is approximately linear, it can be fit via linear least squares to provide a method to predict the momenta difference between the perturbed motion and the reference torus at any time. The function output by linear least squares is summarized in Table 8.

Table 8: Intercept and Slope for Torus #1 Momenta Differences at a Given Time Via Linear Least Squares

Momentum Difference	500 TU @ $\Delta t = 0.25$ TU		6000 TU @ $\Delta t = 0.25$ TU	
	Intercept	Slope	Intercept	Slope
$\delta\mathbf{P_1}$	9.805×10^{-7}	-1.935×10^{-7}	9.778×10^{-6}	-1.950×10^{-7}
$\delta\mathbf{P_2}$	8.300×10^{-7}	-1.507×10^{-7}	8.074×10^{-6}	-1.527×10^{-7}
$\delta\mathbf{P_3}$	9.511×10^{-7}	-1.766×10^{-7}	9.179×10^{-6}	-1.781×10^{-7}

In the case of the momenta, the intercept and slope values are fairly independent of the integration duration. The momenta differences between the reference torus and the perturbed motion can easily be calculated as

$$\delta \mathbf{P}(t) = \delta \mathbf{P}_{intercept} + \delta \mathbf{P}_{slope} t \tag{85}$$

where $\delta \mathbf{P}_{intercept}$ is the linear least squares intercept for $\delta \mathbf{P}$ and $\delta \mathbf{P}_{slope}$ is the linear least squares slope for $\delta \mathbf{P}$.

For all three cases, over time, the momenta difference drifts negatively and linearly. The drift is clearly visible in Figure 28 and Figure 29.
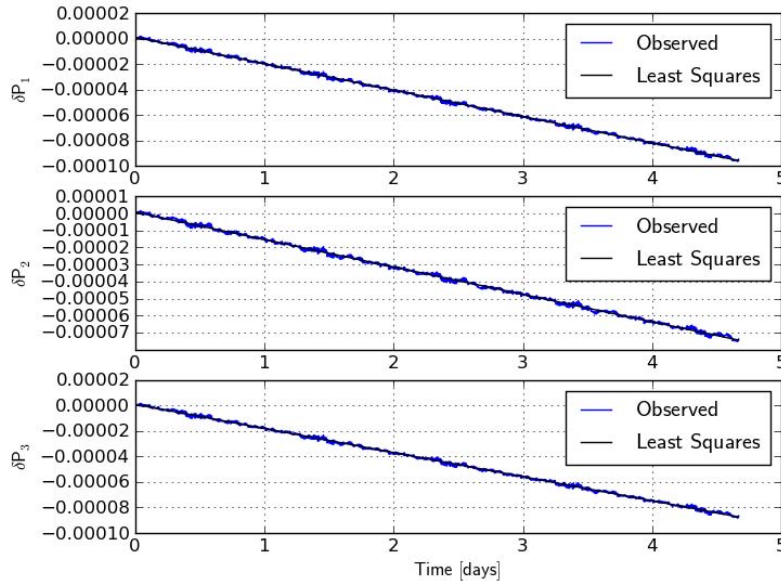
Figure 28: Momenta Differences and Linear Fits for 4.5 Days

For long term position error, this infers that the state error due to instantaneous momenta offsets will be unbounded over time if just coordinate updates are performed. The decreasing slopes are representative of the fact that momenta are energy-like terms which would be expected to decrease over time in the presence of the non-conservative force due to air drag. These insights are associated with the necessary
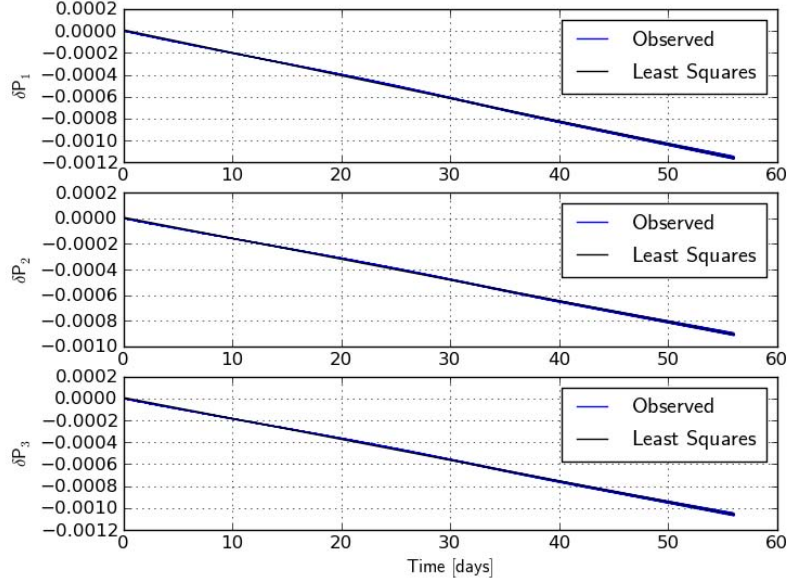
Figure 29: Momenta Differences and Linear Fits for 56 Days

conclusion that despite coordinate updates/prediction, a KAM Torus can only provide accurate state prediction for a satellite encountering drag for a finite time – unless momenta differences, $\delta\mathbf{P}$, even though small, can be accounted for.

4.3.4   Differences Due to Time Period of Concern.   As discussed in §§4.3.3-4, the slopes of the linear least square lines vary slightly depending on the time duration of the data that was fit. Additionally, in the case of the coordinate Q_3, the slope even changes directions between the 4.5 day and 56 day cases of the coordinate time derivative differences and coordinate phase per time predictions. These slope differences are caused mostly by long-periodic behavior in the coordinates. This long-periodic behavior is clearly seen in Figure 30. Phase and momenta difference plots for the 280 day case are located in Appendix A, Figures 54 and 55, respectively.

Short-term fits may place emphasis on a peak or trough of the periodic behavior. As a consequence, when utilizing coordinate update techniques it must be determined what period of time is of interest. If the KAM torus is to be reconstructed every

60
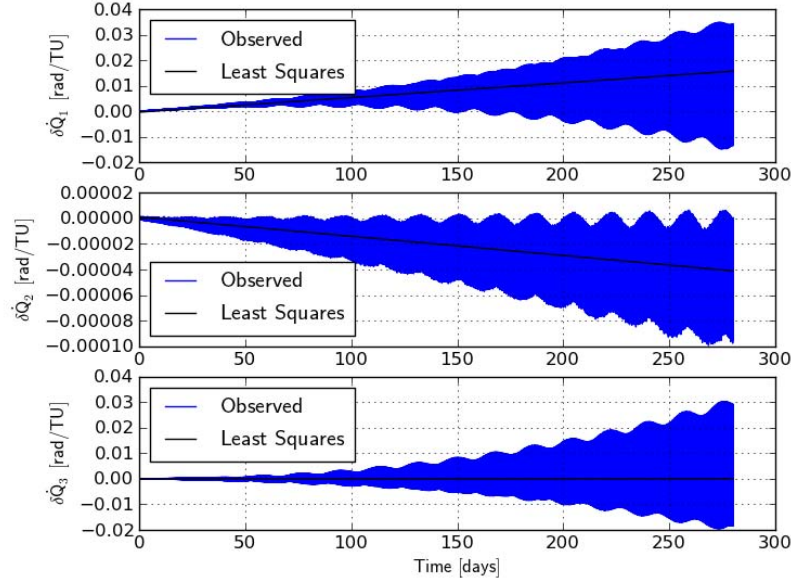
Figure 30: Coordinate Time Derivative Differences and Linear Fits for 280 days

couple of days, the near-term fit will provide better accuracy. Otherwise, if the KAM torus is to be constructed and utilized for long time periods the long-term fit should be used. If both near-term and long-term accuracy are required, it may be possible to schedule prediction curves. The coordinate prediction would initialize with the near-term prediction line and switch to the long-term prediction line at a specified, predetermined, elapsed time.

4.3.5 Application to Any Earth Satellite Torus. Once the coordinates and momenta have been characterized as a function of time, they can simply be added to the propagation loop in future KAM torus algorithms. The functions are unique because they are dependent on satellite configuration, altitude and air density, and orbit eccentricity. It is possible that in the future a database could be established that provides coordinate and momenta functions for common orbit cases.

The author envisions that functions would be available for orbits classified per semi-major axis, eccentricity, and inclination. The functions could be normalized via

some nominal ballistic coefficient then modified per the actual ballistic coefficient. A brief survey was performed to determine the feasibility of such an approach.

The differences in coordinate rates, phase histories, and differences in momenta were again fit via linear least squares as in the previous sections, but three additional cases were evaluated in which the ballistic coefficient value was varied. The results of the drag coefficient survey are summarized in Table 9.

Table 9: Torus Variable Fit Slopes for Various Ballistic Coefficients

	$B^* = 0.01$ Fit Slope	$B^* = 0.02$ Fit Slope	$B^* = 0.05$ Fit Slope	$B^* = 0.1$ Fit Slope
$\delta\dot{Q}_1$	1.195×10^{-7}	2.392×10^{-7}	6.008×10^{-7}	1.213×10^{-6}
$\delta\dot{Q}_2$	-3.125×10^{-10}	-6.288×10^{-10}	-1.587×10^{-9}	-3.190×10^{-9}
$\delta\dot{Q}_3$	-4.711×10^{-11}	2.144×10^{-10}	1.288×10^{-9}	2.783×10^{-9}
Φ_{Q1}/t	2.441×10^{-7}	4.846×10^{-7}	1.210×10^{-6}	2.431×10^{-6}
Φ_{Q2}/t	-5.649×10^{-10}	-1.189×10^{-9}	-3.072×10^{-9}	-6.247×10^{-9}
Φ_{Q3}/t	-3.478×10^{-9}	-2.624×10^{-9}	-2.773×10^{-11}	4.423×10^{-9}
δP_1	-1.935×10^{-7}	-3.877×10^{-7}	-9.747×10^{-7}	-1.968×10^{-6}
δP_2	-1.507×10^{-7}	-3.019×10^{-7}	-7.592×10^{-7}	-1.533×10^{-6}
δP_3	-1.766×10^{-7}	-3.539×10^{-7}	-8.898×10^{-7}	-1.797×10^{-6}

In summary of the data in Table 9, the slopes of the linear fits for nearly all parameters are related such that the fit slope is nearly proportional to the ballistic coefficient. Again, the coordinate Q_3 seems to be behaving in a different manner. At some point in the ballistic coefficient sweep, the parameters associated with Q_3, $\delta\dot{Q}_3$ and Φ_{Q3}/t, transition from a decreasing slopes to increasing slopes. The cause is again related to short and long term periodic behavior.

The results listed in Table 9 are summarized graphically in Figure 31, Figure 32, and Figure 33 with the exception that the linear fits of the $B^* = 0.02$ case were removed for clarity:
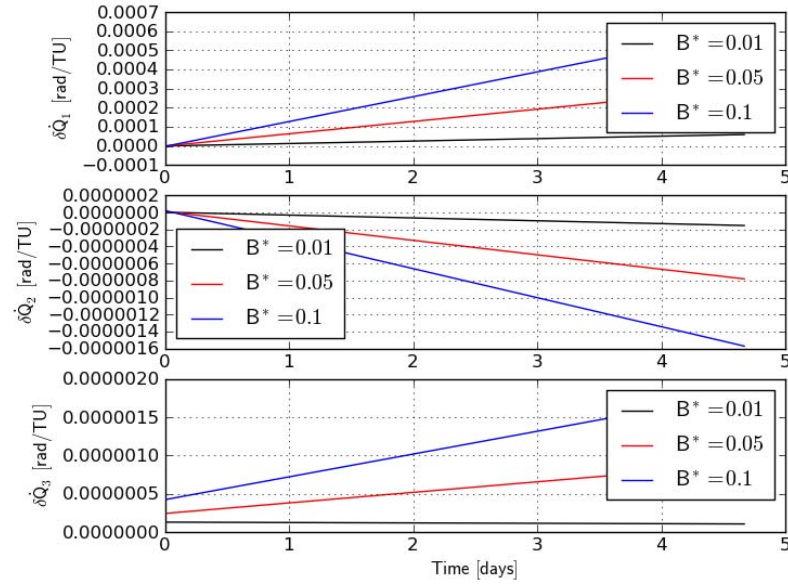
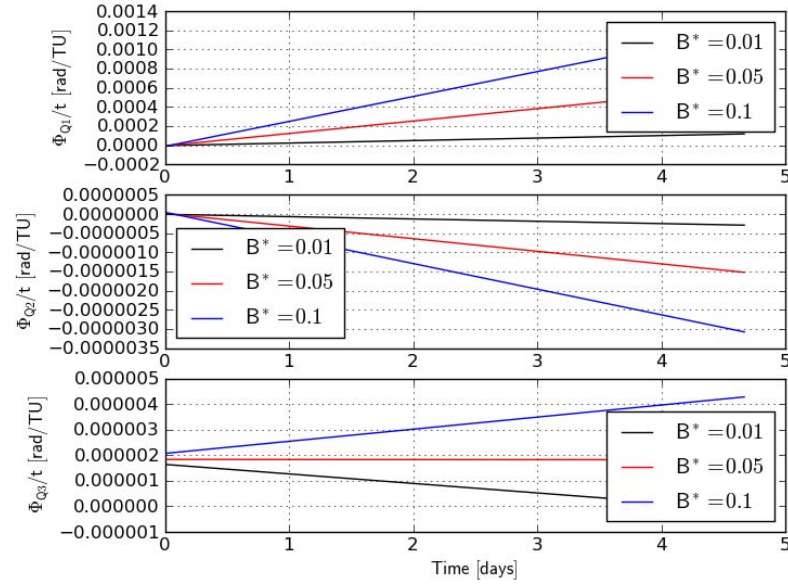Figure 31: Linear Fits of Coordinate Time Derivative Differences for Various B* Values

Figure 32: Linear Fits of Coordinate Phase for Various B* Values

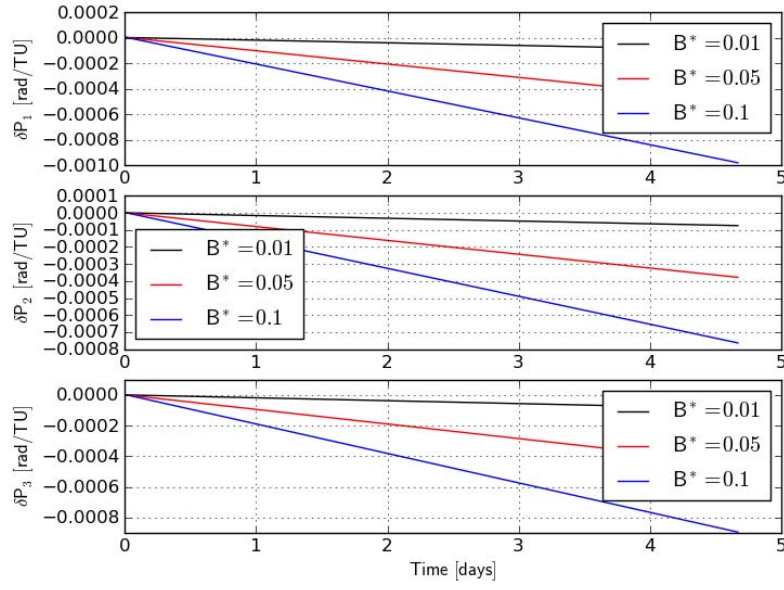Figure 33: Linear Fits of Momenta Differences for Various B* Values

4.4 Methods to Characterize Third-Body Lunar Effects on KAM Torus Coordinates and Momenta

Previous data, plots, and discussions on third-body lunar effects on torus coordinates and momenta have primarily focused on data over a time of 500 TU or just over 4.5 days. Because the Moon's orbital period about the Earth is about 27 days and the force of the Moon's gravity on the satellite is clearly a function of the geometry between the satellite and the Moon, it is reasonable to suspect that data spanning one or more moon period is required to uncover the entirety of the third-body behavior. Thus a time period of 6000 TU or about 56 days was chosen for additional data collection.

The changes in phase required to keep the reference torus aligned with the lunar perturbed motion appears to be symmetrical but there is non-negligible accumulation of phase over the long term. The phase over time exhibits a periodic-like behavior and is illustrated in Figure 34:
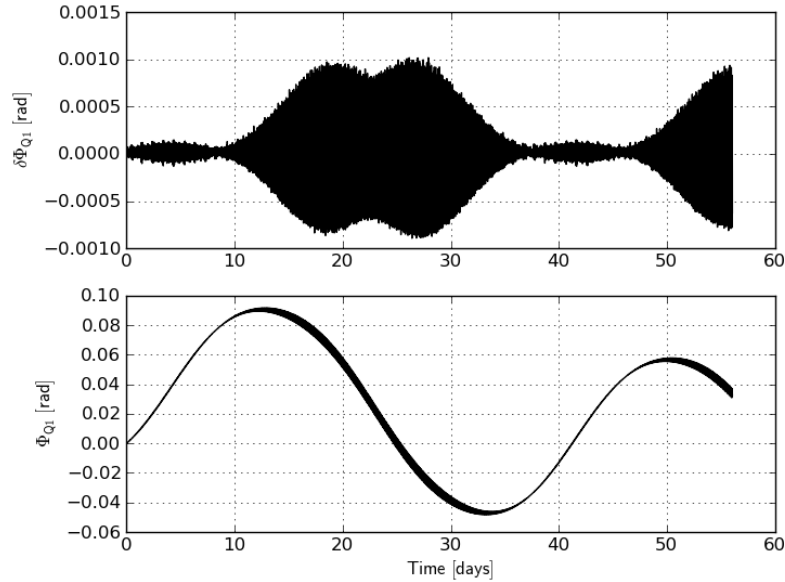
Figure 34: Coordinate Q1 Phase Differences and Phase History for Lunar Case

It is observed that after one period, the phase doesn't return to the starting value. This discrepancy is at least partially caused by the error/offset shown in the baseline case, shown in Figure 35:
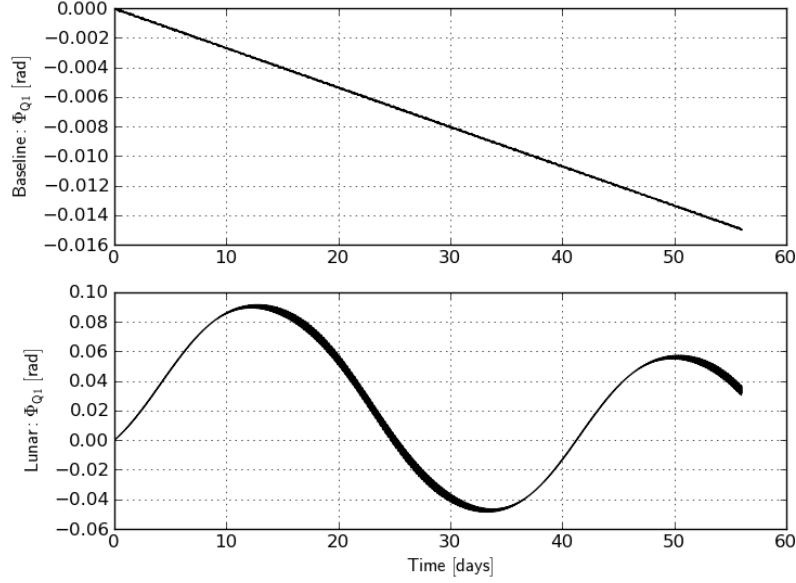
Figure 35: Comparison of Q1 Phase History of Baseline and Lunar Cases

From Figure 35 it can be determined about half of the offset in the lunar case can be explained by the baseline offset. Coordinate Q_3 phase shows similar behavior to that of Q_1 phase except that the Q_3 phase returns to the same value after one period as shown in Figure 36.

The phase of coordinate Q_2 behaves much differently than the other coordinates in that while still showing periodic behavior, the phase is nearly constantly decreasing. The phase difference and history of Q_2 is shown in Figure 37.
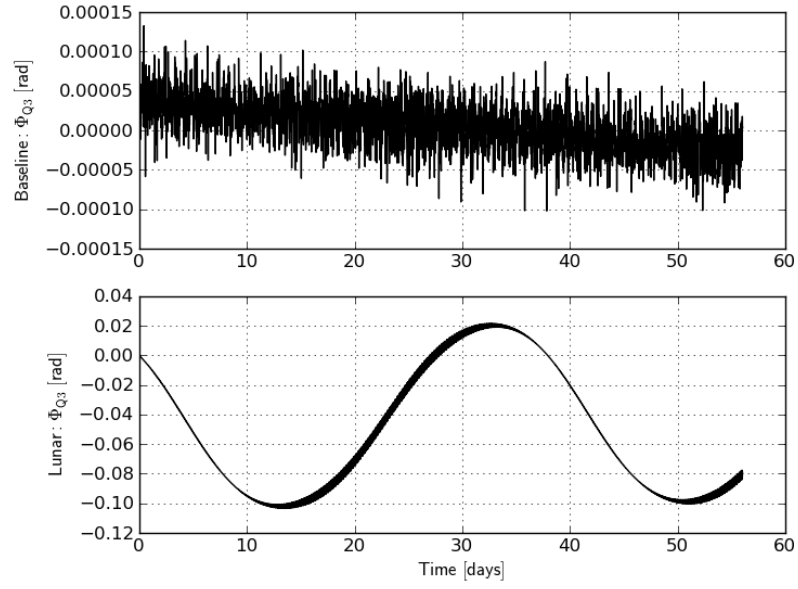
Figure 36: Coordinate Q3 Phase History for Baseline and Lunar Cases
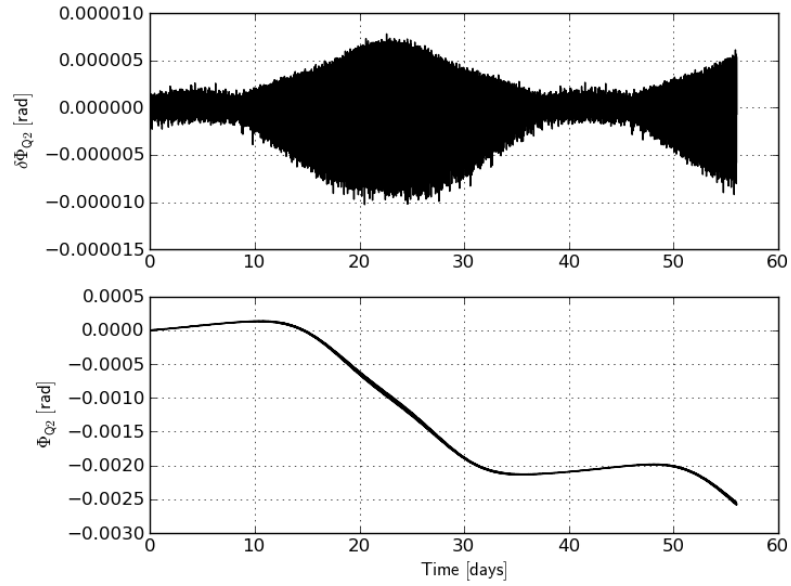
Figure 37: Coordinate Q2 Phase Differences and Phase History for Lunar Case

67

In the case that lunar perturbed motion was being compared to a reference torus and the coordinate phases were not being tracked and updated with time the error in Q_2 would grow unbounded while the error in the other two coordinates would significantly oscillate and grow slowly. The momenta differences in the lunar case show significant behavior. All three exhibit periodic behavior with a period of about 37 days. Within this time period, the momenta differences return to zero twice, as seen in Figure 38. Both zero crossings are explained by symmetry. When the simulation of the Moon's third-body effects begins, some angular offset, less than π radians, between the satellite's RAAN, AP, and the Moon's position about the Earth exists. The first zero crossing is explained by this initial angle being reduced to zero and then duplicated on the "other side". The second zero crossing is then explained by the Moon-RAAN-AP system completing an entire period.
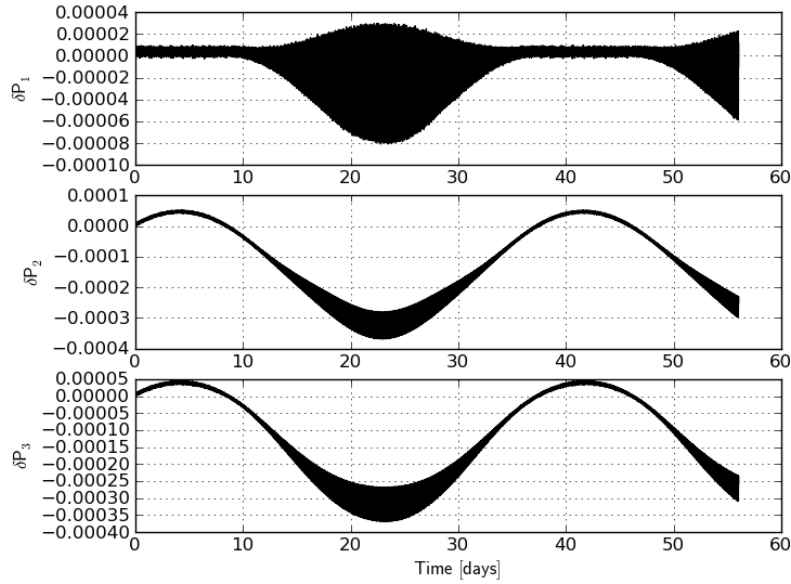
Figure 38: Momenta Differences for Lunar Case

The 37 day period is also clearly seen in the total position and velocity error plots shown in Figure 39. The occurrence of zero error points aligning with the zero

momenta difference points in Figure 38 is not a surprise. Because this analysis requires the coordinates be updated to account for phase differences (so that ultimately the linear transformation via the Jacobian is valid), the only contributor to error is necessarily momenta differences. When the momenta differences between the perturbed motion and the reference torus return to zero the error also returns to zero. Obtaining this accuracy, even at two specific points in time, is difficult in practice.
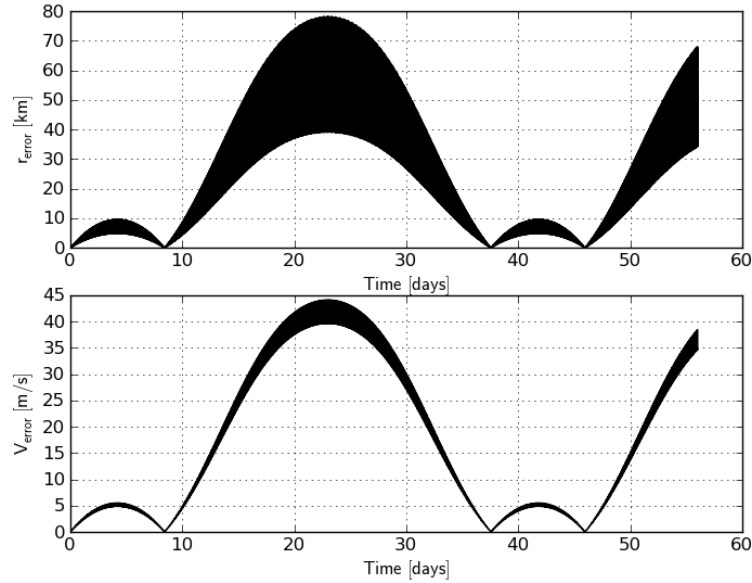

Figure 39: Total Position and Velocity Error Between Reference Torus and Perturbed Motion for Lunar Cases

Per Figure 38 and Figure 39 in which the system period appears to be about 37 days, the approximate frequency can be estimated as

$$\omega_{ls-est} = \frac{2\pi}{\mathcal{P}} = \frac{2\pi}{37 day \cdot 107.09 TU/day} = 0.001586 \frac{rad}{TU} \tag{86}$$

where ω_{ls-est} is the estimated lunar system frequency, and $\mathcal{P}$ is the period of the combined frequency system.

69

As illustrated in Figure 40, the system frequency is a function of $\dot{Q}_2$, $\dot{Q}_3$, and ω_{moon}.
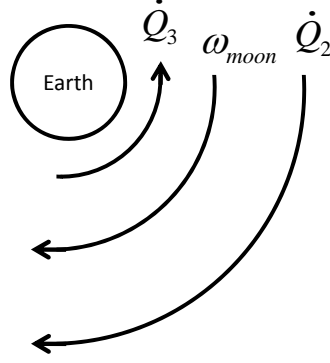
Figure 40: Earth Satellite and Third-Body Lunar Frequencies in the ECEF Frame

Per the relationship defined in Figure 40, Equation 87 specifies the system frequencies observed in Figure 38 and Figure 39 as

$$\omega_{ls} = \dot{Q}_2 - \omega_{moon} + \dot{Q}_3 \tag{87}$$

where ω_{ls} is the frequency of the lunar system.

The lunar system frequency is a function of the frequency of the second and third reference torus coordinates as well as the frequency of the moon, all in the ECEF frame. The frequencies and periods are summarized in Table 10:

Table 10: Earth Satellite Perturbed by Lunar Effects System Frequencies

	$\dot{Q}_2$	$\dot{Q}_3$	ω_{moon}	ω_{ls}
Frequency rad/TU	-0.059833	0.001586	-0.056683	-0.001564
Period TU	105.01	3961.66	110.85	4017.38

The result of 4017.38 TU or 37.5 days for the combined period is equivalent to the time picked directly off the momenta differences and total error plots.

70

It has been shown that predicting the coordinate phases is not trivial because the trends show periodic characteristics but do not return to previous values in the case of Q_1 and Q_2. Also, it must be remembered that the Moon model utilized in this research was simplified. To utilize this approach in operational applications, a more accurate Moon model would need to be used, and in particular the initial state of the Moon would have to align with reality rather than arbitrarily established.

With the complex characteristics uncovered regarding the Moon's effect on motion near a reference torus, an important realization is made: if possible the application of KAM Theory to Earth satellites should be expanded to include the Moon in the dynamics when constructing a KAM torus. There are two major reasons this approach may be viable: 1) the motion near the reference torus is seen to be affected by specific frequencies that are functions of current KAM torus frequencies as well as the Moon's orbital frequency (Bordner (2) also saw frequencies due to third-body Moon effects in his analysis of GPS satellite tori), and 2) the forces applied to an Earth orbiting satellite by the moon are conservative.

Beyond evidence showing it may be possible, there is also significant motivation to include the moon in KAM torus construction. First, this research has shown that especially in the short term, lunar effects can cause more state error than air drag – specifically seen in the case of Torus #1. The maximum state error due to the Moon is on the order of 80 km and 40 m/s for the analyzed case which has benefited from phase updates to the coordinates after every time step.

The second motivation is that to predict and update the coordinates would be a significant effort, unique to any orbit at any time. In practice, the requirements would essentially be on par with special perturbation theory, which opposes the goals of applying KAM tori to Earth satellites. While complex to initially formulate, the

new KAM torus including the Moon's dynamics will most likely be adjacent to the previous KAM torus and will have additional basis frequency/momentum pairs.

V. Conclusion

5.1   Results

This research has realized several key results that will help to further the application of KAM Theory to Earth orbiting satellites. The motion of a satellite perturbed by atmospheric air drag or third-body lunar gravity effects was compared to the motion predicted by a reference orbit characterized by a KAM Torus. It was shown that KAM Theory isn't precluded in these perturbing situations, but certain considerations must be made. Primary results include:

- Obtaining an accurate Jacobian is critical. The quality of the Jacobian can be greatly enhanced beyond that of the 2BP approximation by updating the first three columns of $\frac{\partial \mathbf{X}}{\partial \mathbf{Y}}$ with data extracted directly from the KAM torus, $\frac{\partial \mathbf{q}}{\partial \mathbf{Q}}$ and $\frac{\partial \mathbf{p}}{\partial \mathbf{Q}}$. Methods should be developed to more accurately approximate the last three columns of the Jacobian, $\frac{\partial \mathbf{q}}{\partial \mathbf{P}}$ and $\frac{\partial \mathbf{p}}{\partial \mathbf{P}}$.

- The linear transformation performed via the Jacobian is only valid when the reference torus coordinates are closely aligned with the equivalent coordinates of the perturbed motion. The coordinate alignment can be characterized as a set of phases that are updated over time.

- Given an Earth satellite's state and drag characteristics, functions of time can be numerically derived to approximate and predict air drag's effects on the reference torus coordinates and momenta. Described in the torus variables, air drag primarily affects the first and third coordinates which are approximately equivalent to the mean anomaly and argument of perigee, respectively. Momenta differences cause unbounded error over time inferring that at some point in time, dependent on application, the current torus characterization will become invalid.

- Moon third-body effects cause significant near-term state error. In the long term, some of the Moon's effects average out in a specific period of time determined

by the Moon's orbital frequency and the KAM Torus' second and third basis frequencies. Characterizing the Moon's effects on motion near a reference KAM torus at any given time will require complex effort of similar specificity to that of special perturbation theory if the current method is employed.

5.2 Future Efforts and Recommendations

Though several key results have been realized, as in most pursuits of advancement, more work needing attention has been uncovered. The motivation for this research was to contribute to a new method of orbit characterization and prediction. Current day techniques are not adequate to predict, let alone prevent, the catastrophic collisions of artificial satellites that will most likely hamper, if not deny, humanity's access to space in the future. With consideration to the lofty goal of improving upon the methods used for decades to track and predict Earth satellite motion but also with the focus pertinent to this body of research, the following future efforts are recommended.

- Develop a database of coordinate change prediction functions due to air drag with a standard, baseline ballistic coefficient. The database would most likely provide coordinate updates in terms of linear functions defined by intercepts and slopes for various classes of orbits. Orbit classes should be determined by a combination of semi-major axis, eccentricity, and inclination. Potentially, the orbit classes could also be defined by torus coordinate basis frequencies.
- Study the relationship between ballistic coefficient values and the slope of the coordinate time derivative prediction. Based on the author's brief survey, the relationship appears mostly linear with small quadratic correction terms.
- Develop an approach for "jumping" to an adjacent torus when momenta differences become too large.

- Incorporation of the Moon's third-body effects as additional coordinate-momentum pairs in KAM Torus construction should be investigated. The periodic nature of the phase accumulation and the momenta differences seen in the lunar cases leads the author to believe this approach is promising. Incorporating the Moon in KAM Torus construction would also remove the necessity of the complex operations required to predict the Moon's state over time for input into third-body force calculations.

Appendix A.   Additional Figures and Tables

Table 11: Comparison of Portion of Jacobian Approximated by Two-Body Problem
and Exact Values from Torus #2

Two-Body Jacobian			Partial Torus Extraction Jacobian		
3.672096e-1	8.270228e-2	3.661185e-1	3.674205e-1	8.271854e-2	3.668758e-1
-9.654751e-1	-6.826067e-1	-9.638614e-1	-9.664381e-1	-6.824581e-1	-9.655660e-1
2.132824e-1	5.787414e-14	2.134467e-1	2.133621e-1	2.304481e-5	2.133971e-1
6.326216e-1	8.924565e-1	6.318474e-1	6.319386e-1	8.924208e-1	6.315438e-1
7.664626e-2	3.394376e-1	7.717644e-2	7.678464e-2	3.394487e-1	7.700849e-2
-7.390048e-1	-3.893083e-14	-7.384972e-1	-7.394273e-1	1.266063e-4	-7.391464e-1
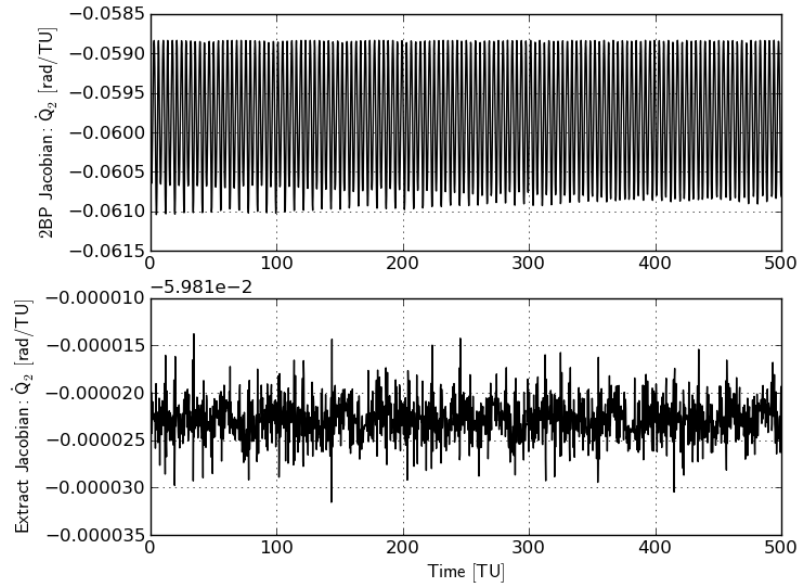
Figure 41: Time Derivative of Unperturbed Torus Coordinate Q_2 Utilizing the Two-
Body Jacobian and the Partial Torus Extraction Jacobian
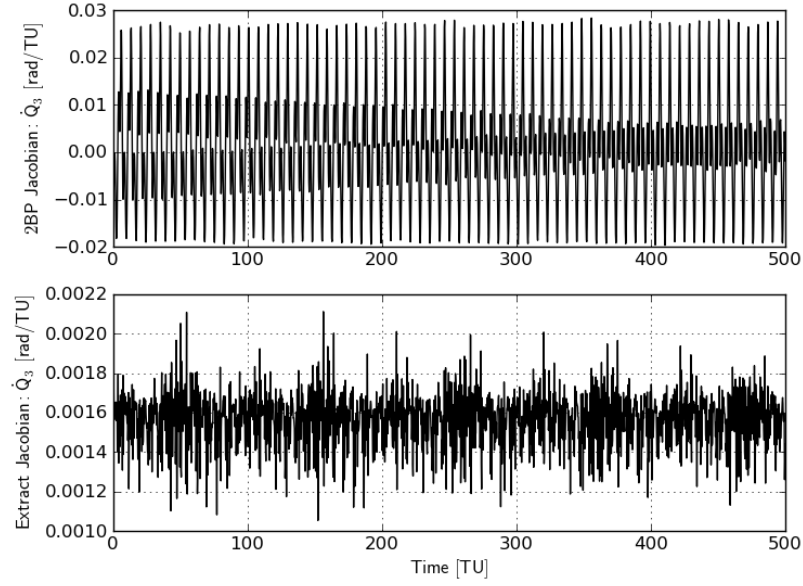
Figure 42: Time Derivative of Unperturbed Torus Coordinate Q_3 Utilizing the Two-Body Jacobian and the Partial Torus Extraction Jacobian
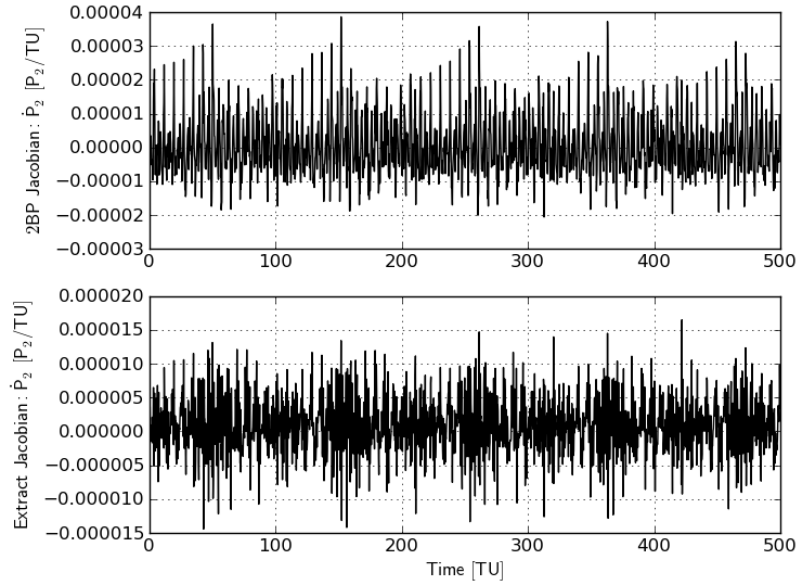
Figure 43: Time Derivative of Unperturbed Torus Momentum P_2 Utilizing the Two-Body Jacobian and the Partial Torus Extraction Jacobian
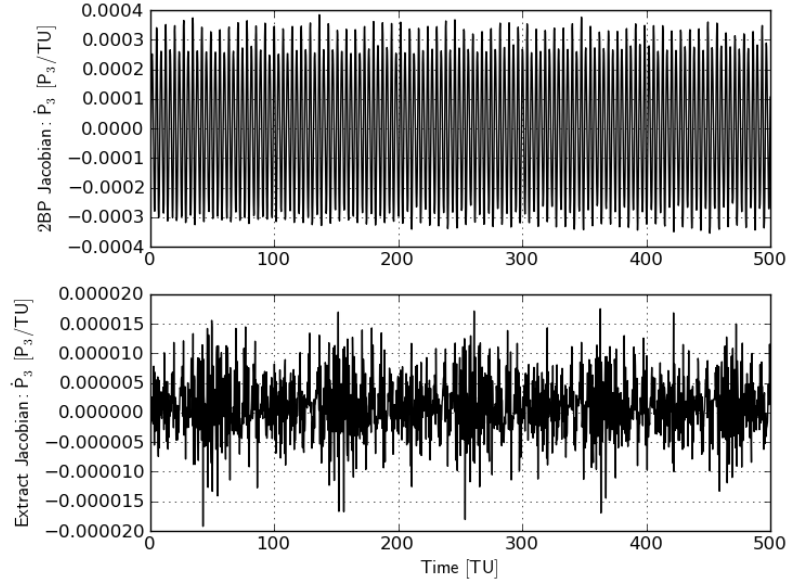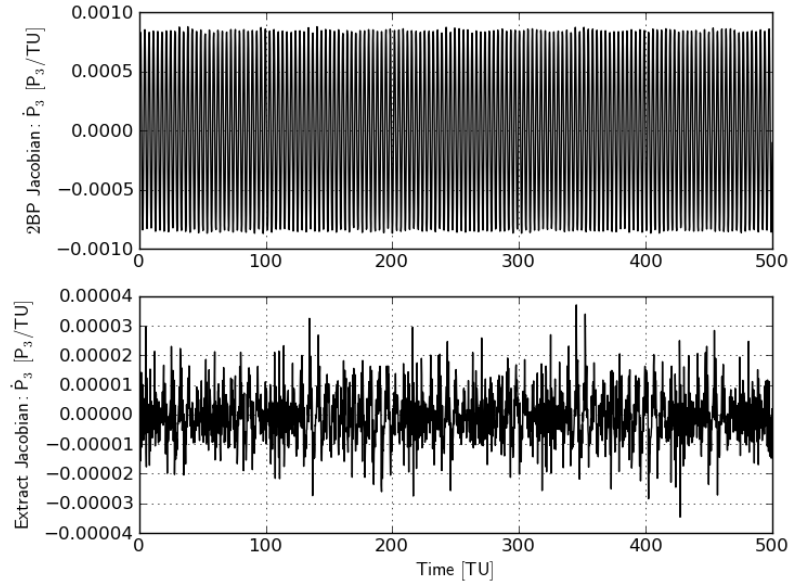
Figure 44: Time Derivative of Unperturbed Torus Momentum P_3 Utilizing the Two-Body Jacobian and the Partial Torus Extraction Jacobian
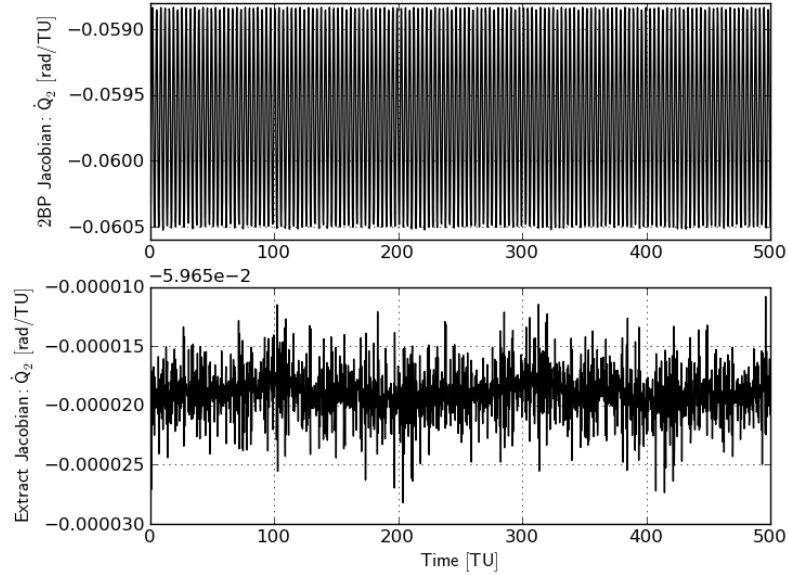

Figure 45: Time Derivative of Unperturbed Torus #2 (ISS) Coordinate Q_2 Utilizing the Two-Body Jacobian and the Partial Torus Extraction Jacobian
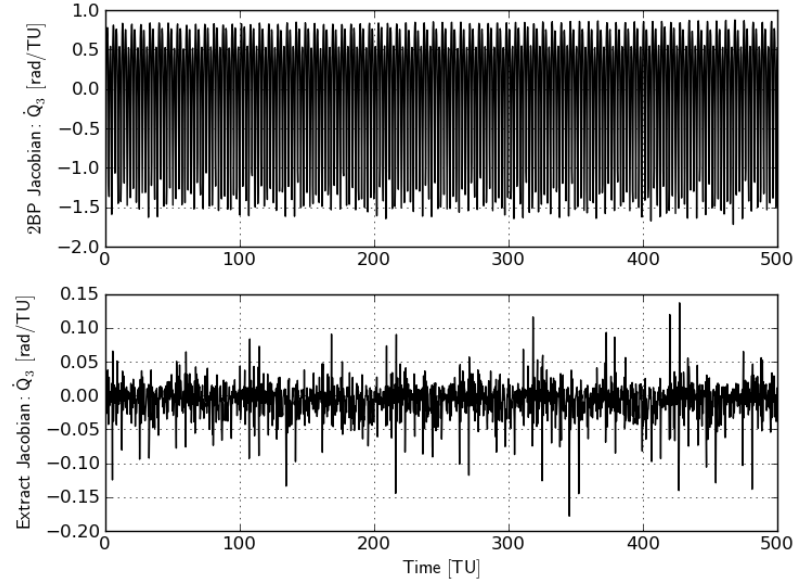
Figure 46: Time Derivative of Unperturbed Torus #2 (ISS) Coordinate Q_3 Utilizing the Two-Body Jacobian and the Partial Torus Extraction Jacobian
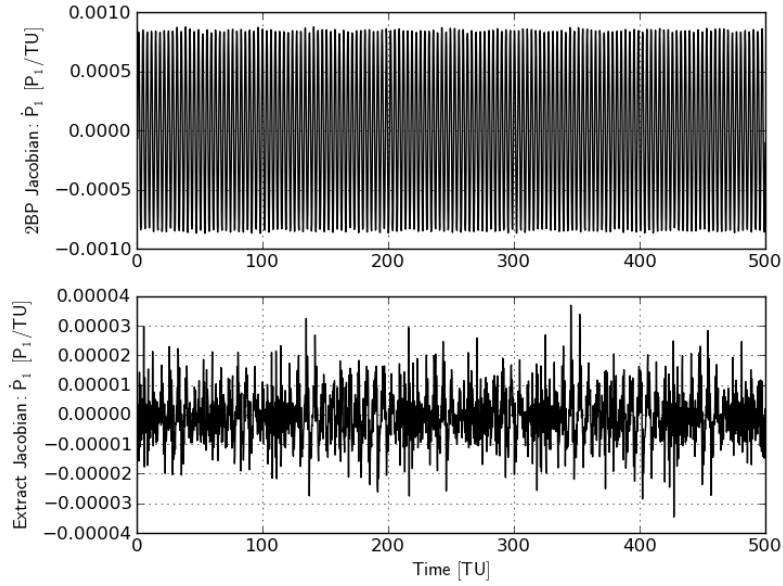
Figure 47: Time Derivative of Unperturbed Torus #2 (ISS) Momentum P_1 Utilizing the Two-Body Jacobian and the Partial Torus Extraction Jacobian
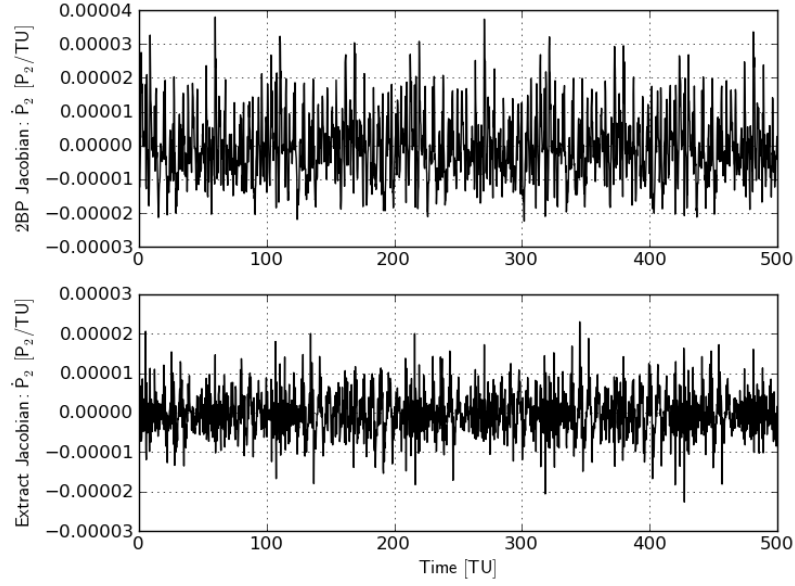
Figure 48: Time Derivative of Unperturbed Torus #2 (ISS) Momentum P_2 Utilizing the Two-Body Jacobian and the Partial Torus Extraction Jacobian

Figure 49: Time Derivative of Unperturbed Torus #2 (ISS) Momentum P_3 Utilizing the Two-Body Jacobian and the Partial Torus Extraction Jacobian
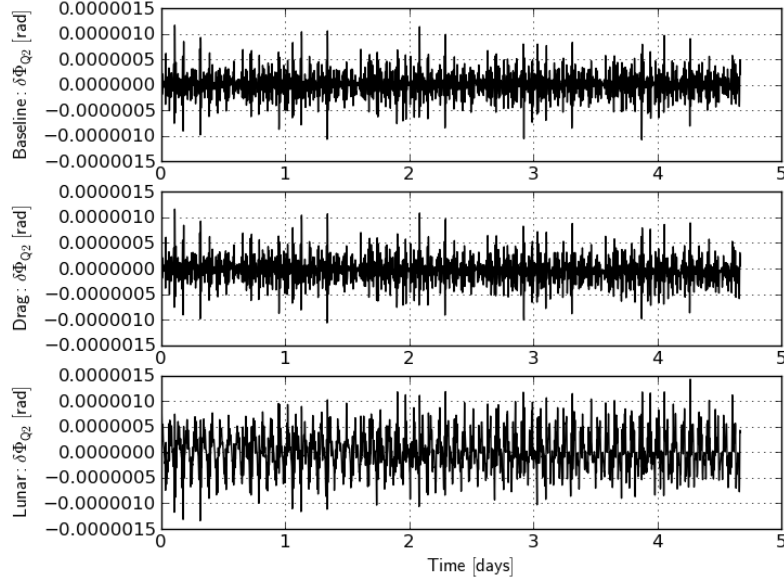
Figure 50: Coordinate Q_2 Phase Differences for Baseline, Drag, and Lunar Cases
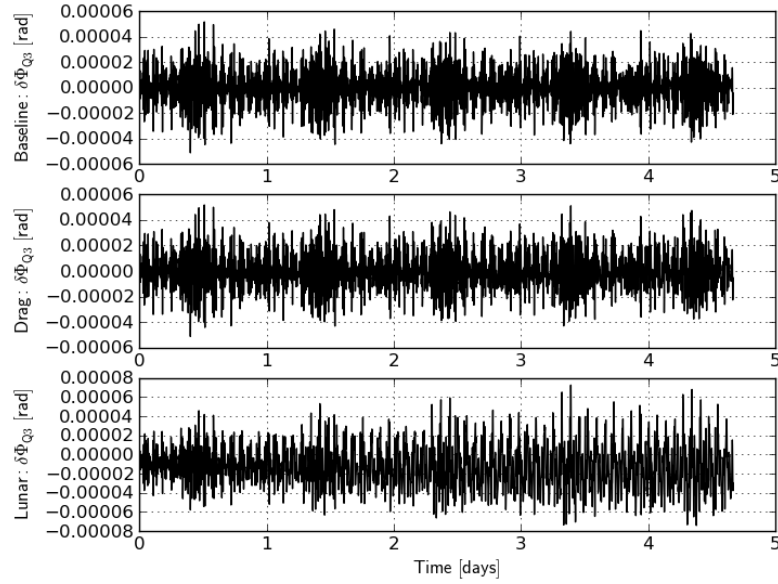
Figure 51: Coordinate Q_3 Phase Differences for Baseline, Drag, and Lunar Cases
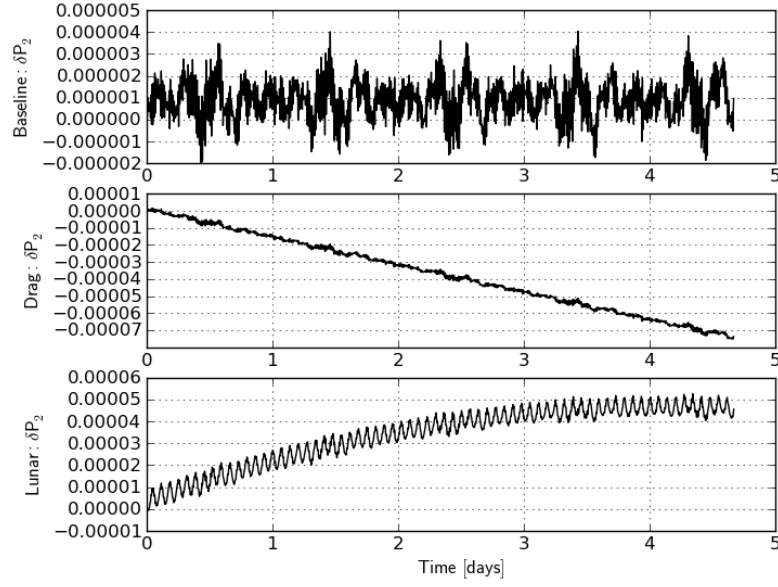
Figure 52: Momentum Differences, δP_2, for Baseline, Drag, and Lunar Cases
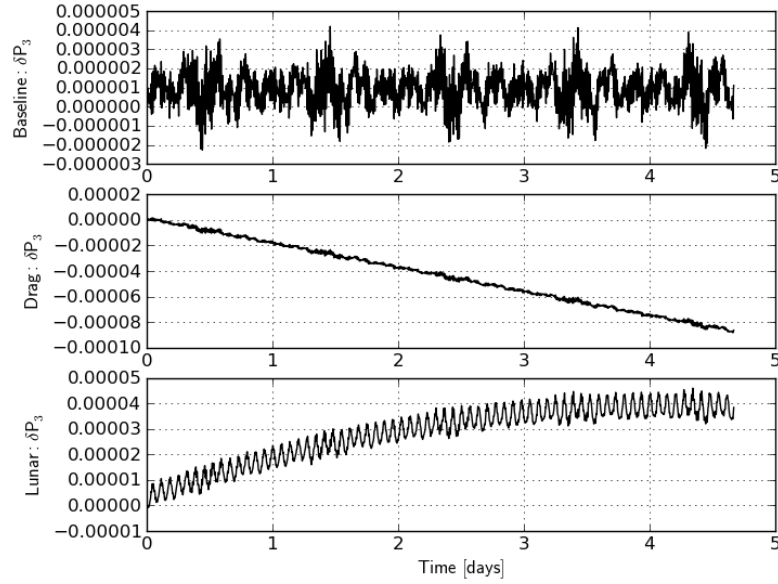
Figure 53: Momentum Differences, δP_3, for Baseline, Drag, and Lunar Cases
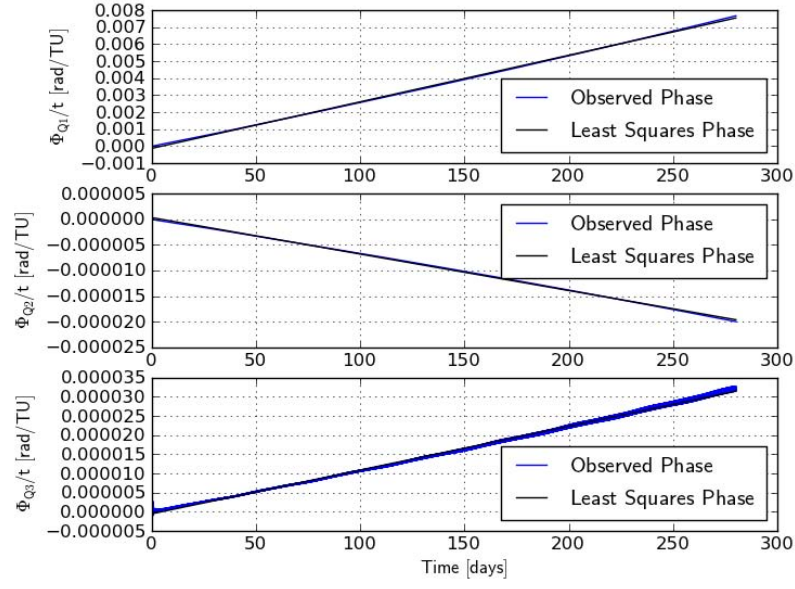
Figure 54: Coordinate Phase Per Time and Linear Fits for 280 days
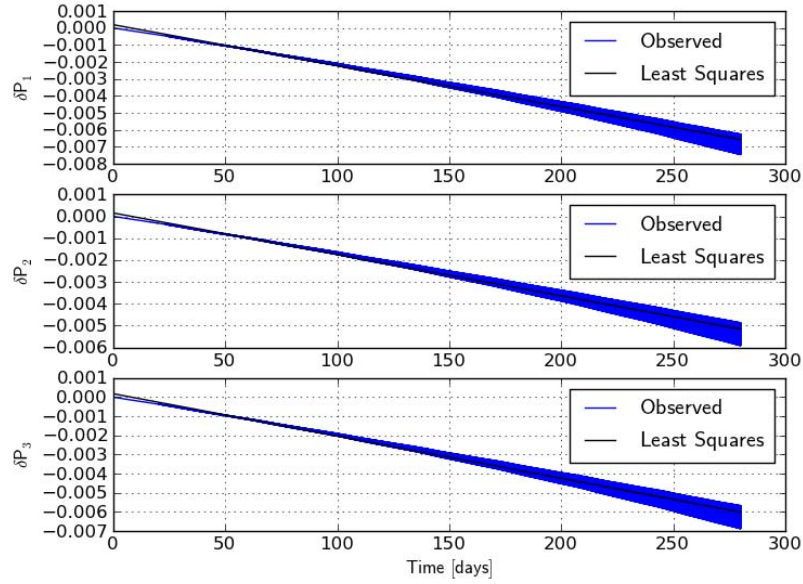
Figure 55: Momenta Differences and Linear Fits for 280 Days
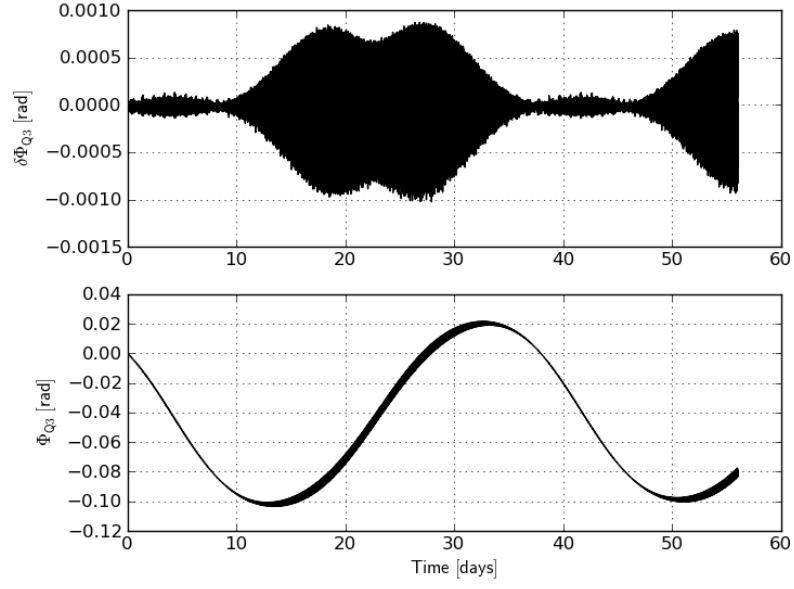
Figure 56: Coordinate Q_3 Phase Differences and Phase History for Lunar Case
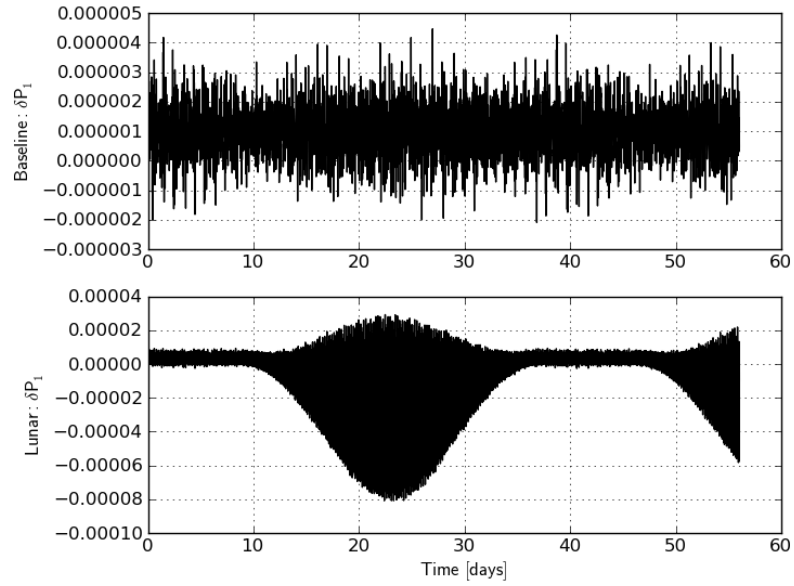
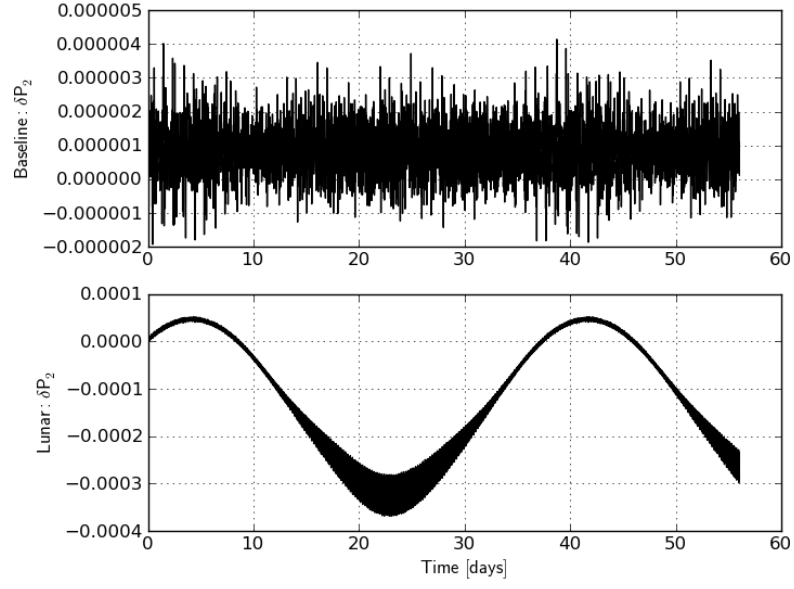Figure 57: Momentum Differences, δP_1, for Baseline and Lunar Cases

84

Figure 58: Momentum Differences, δP_2, for Baseline and Lunar Cases
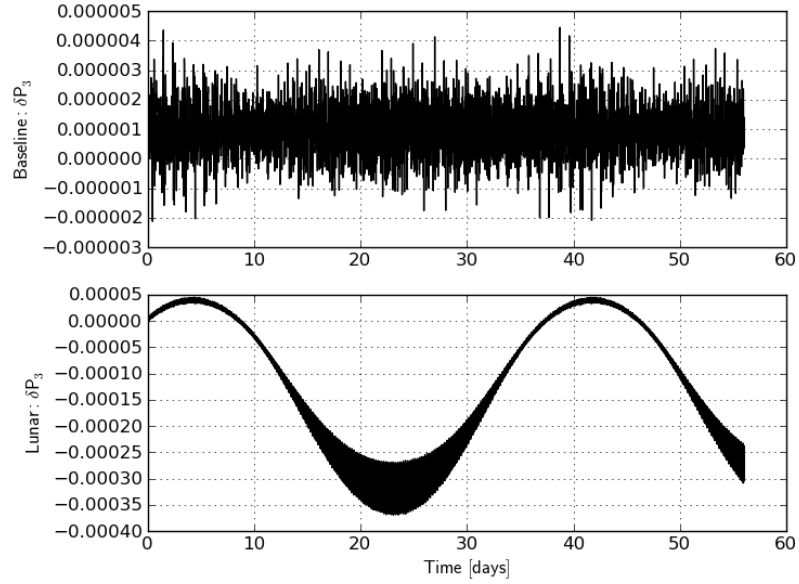

Figure 59: Momentum Differences, δP_3, for Baseline and Lunar Cases
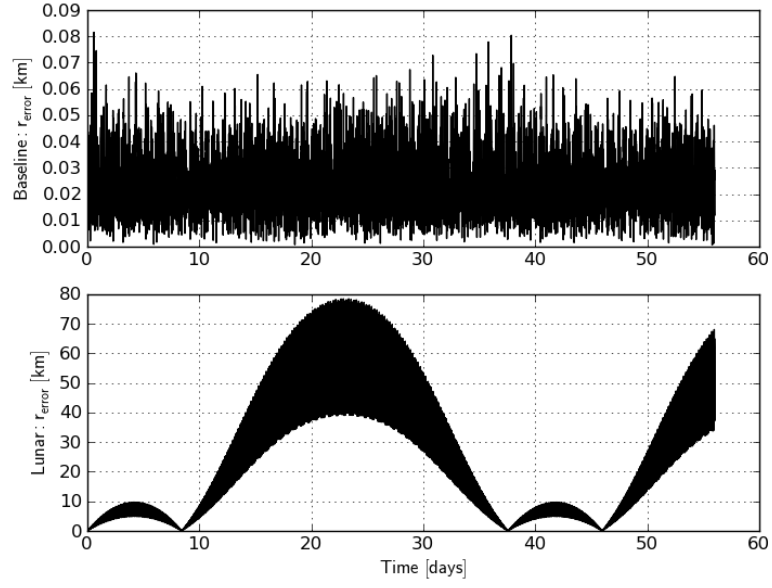
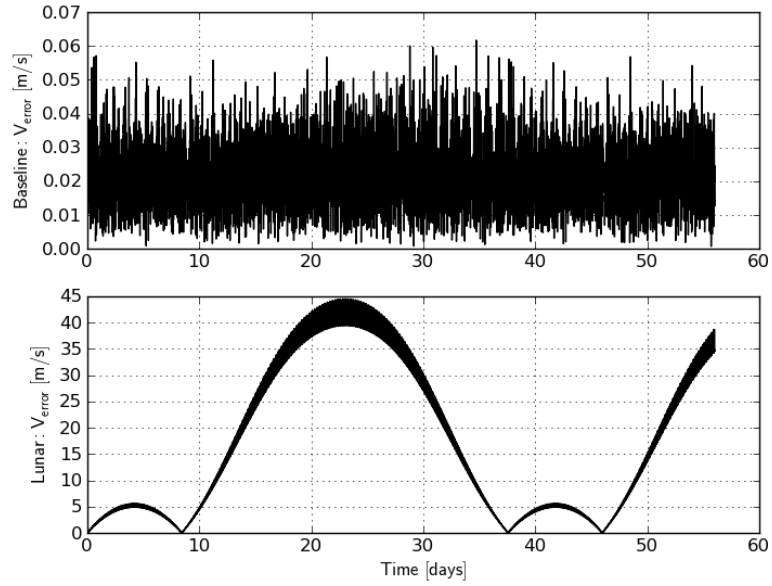Figure 60: Total Position Error for Reference Torus and Perturbed Motion for Baseline and Lunar Cases

Figure 61: Total Velocity Error for Reference Torus and Perturbed Motion for Baseline and Lunar Cases

Bibliography

1. Arnold, Vladimir. "Proof of Kolmogorov's Theorem on the Preservation of Quasi-Periodic Motions Under Small Perturbations of the Hamiltonian". *Russian Mathematical Survey*, 18(N6):9–36, 1963.

2. Bordner, Ralph E. III. *Orbital Tori Construction Using Trajectory Following Spectral Methods*. Ph.D. thesis, Air Force Institute of Technology, 2010.

3. Brouwer, Dirk and Gerald M. Clemence. *Methods of Celestial Mechanics*. Academic Press, Inc., New York, NY, 1961.

4. "Iridium 33/Cosmos 2251 Collision", September 2010. URL `http://www.celestrak.com/events/collision/`.

5. Chao, Chia-Chun. *An Analytical Integration of the Averaged Equations of Variation Due to Sun-Moon Perturbations and Its Application*. Technical Report TR-80-12, The Aerospace Corporation, El Segundo, CA, 1979.

6. Chao, Chia-Chun "George". *Applied Orbit Perturbation and Maintenance*. The Aerospace Press, El Segundo, CA, 2005.

7. Chobotov, Vladmir A. (editor). *Orbital Mechanics*. American Institute of Aeronautics and Astronautics, Inc., 3rd edition, 2002.

8. Craft, Christopher. *Formation Flight of Earth Satellites on KAM Tori*. Master's thesis, Air Force Institute of Technology, 2009.

9. Kaufman, B. "Variation of Parameters and Long-Term Behavior of Planetary Orbits", 1970. AAS/AIAA Astrodynamics Conference.

10. Kelso, T.S., January 2011. URL `http://twitter.com/TSKelso`.

11. Kolmogorov, Andrey. "On the Conservation of Conditionally Periodic Motions Under Small Perturbations of the Hamiltonian". *Doklady Akademii Nauk SSSR*, 98:469, January 1954.

12. Little, Bryan D. *Application of KAM Theorem to Earth Orbiting Satellites*. Master's thesis, Air Force Institute of Technology, 2009.

13. Moser, Jürgen. "On Invariant Curves of an Area Preserving Mapping of an Annulus". *Nachrichten der Akademie der Wissenschaften in Gottigen. Mathematisch-Physikalische*, IIa(K1):1–20, January 1962.

14. National Aeronautics and Space Administration, Huntsville, AL. *Space and Planetary Environment Criteria Guidelines for Use in Space Vehicle Development*, 1982 revision edition, 1983.

15. Regan, Frank J. and Satya M. Anandakrishnan. *Dynamics of Atmospheric Re-Entry*. American Institute of Aeronautics and Astronautics, Inc., Washington D.C., 1993.

16. Schaub, Hanspeter and John L Junkins. *Analytical Mechanics of Space Systems*. American Institute of Aeronautics and Astronautics, Inc., Reston, VA, 2nd edition, 2009.

17. Vallado, David A. *Fundamentals of Astrodynamics and Applications*. Microcosm Press, El Segundo, CA, 2nd edition, 2001.

18. Wertz, James R. and Wiley J. Larson (editors). *Space Mission Analysis and Design*. Microcosm Press, El Segundo, CA, 3rd edition, 1999.

19. Wiesel, William E. "Motion Near an Earth Satellite KAM Torus". Unpublished.

20. Wiesel, William E. "Earth Satellite Orbits as KAM Tori", 2007. AAS/AIAA Astrodynamics Specialist Conference.

21. Wiesel, William E., 2010. KAM Software in C++.

22. Wiesel, William E. "Earth Satellite Perturbation Theories as Approximate KAM Tori". *American Astronomical Society*, 10(122), 2010.

23. Wiesel, William E. *Modern Astrodynamics*. Aphelion Press, Beavercreek, OH, 2nd edition, 2010.

24. Yates, Max W., 2010. Personal Correspondence.

1. REPORT DATE *(DD-MM-YYYY)*	2. REPORT TYPE	3. DATES COVERED *(From – To)*
24-03-2011	Master's Thesis	June 2010 – March 2011

4. TITLE AND SUBTITLE	5a. CONTRACT NUMBER
Effects of Air Drag and Lunar Third-Body Perturbations on Motion Near a Reference KAM Torus	5b. GRANT NUMBER
	5c. PROGRAM ELEMENT NUMBER
6. AUTHOR(S)	5d. PROJECT NUMBER
Hagen, Luke J., Captain, USAF	5e. TASK NUMBER
	5f. WORK UNIT NUMBER

7. PERFORMING ORGANIZATION NAMES(S) AND ADDRESS(S)	8. PERFORMING ORGANIZATION REPORT NUMBER
Air Force Institute of Technology Graduate School of Engineering and Management (AFIT/EN) 2950 Hobson Way, Building 640 WPAFB OH 45433-7765	AFIT/GA/ENY/11-M06

9. SPONSORING/MONITORING AGENCY NAME(S) AND ADDRESS(ES)	10. SPONSOR/MONITOR'S ACRONYM(S)
Intentionally left blank	
	11. SPONSOR/MONITOR'S REPORT NUMBER(S)

12. DISTRIBUTION/AVAILABILITY STATEMENT
APPROVED FOR PUBLIC RELEASE; DISTRIBUTION IS UNLIMITED.

13. SUPPLEMENTARY NOTES
This material is declared a work of the U.S. Government and is not subject to copyright protection in the United States.

14. ABSTRACT
The KAM Theory was developed in the 1960s but only in the last decade has it been applied to Earth orbiting satellites. Physical state variables of position and velocity are transformed into KAM Torus variables. The KAM Torus is a geometrical structure similar to that of a multi-dimensional donut. The Earth satellite's motion can be described as traversing the surface of this donut. There are two primary advantages of this transformation: (1) The new generalized coordinates which are analogous with mean anomaly, right ascension of the ascending node, and argument of perigee, increment linearly with time, and (2) Perturbations due to the Earth's geopotential are already embedded in a given torus to an arbitrary geopotential order. This study examines methods to describe perturbed satellite motion near a reference KAM Torus. The perturbations addressed in this thesis are atmospheric air drag and third-body effects from the Moon. Perturbed motion was integrated and compared against the unperturbed reference torus motion. For a sample orbit, expressions were numerically derived that allow the modification of the reference torus to allow prediction of the perturbed motion due to drag. It was shown that in the case of third-body lunar effects, the differences between perturbed motion and the reference torus motion cannot be generalized. Instead, there seems to be both evidence and motivation behind attempting to embed the lunar dynamics in the construction of Earth satellite KAM Tori.

15. SUBJECT TERMS
KAM tori, orbital tori, orbital perturbations, air drag, third-body

16. SECURITY CLASSIFICATION OF:			17. LIMITATION OF ABSTRACT	18. NUMBER OF PAGES	19a. NAME OF RESPONSIBLE PERSON
a. REPORT	b. ABSTRACT	c. THIS PAGE			Dr. William E. Wiesel (ENY)
U	U	U	UU	111	19b. TELEPHONE NUMBER *(Include area code)* (937) 255-6565, x4312; william.wiesel@afit.edu